

Versatile Atomic Magnetometry Assisted by Bayesian Inference

R. Puebla,^{1,2} Y. Ban,^{3,4} J. F. Haase,^{5,6} M. B. Plenio,⁷ M. Paternostro,² and J. Casanova^{3,8}

¹*Instituto de Física Fundamental, IFF-CSIC, Calle Serrano 113b, 28006 Madrid, Spain*

²*Centre for Theoretical Atomic, Molecular and Optical Physics,
Queen's University Belfast, Belfast BT7 1NN, United Kingdom*

³*Department of Physical Chemistry, University of the Basque Country UPV/EHU, Apartado 644, 48080 Bilbao, Spain*

⁴*School of Materials Science and Engineering, Shanghai University, 200444 Shanghai, China*

⁵*Institute for Quantum Computing, University of Waterloo, Waterloo, Ontario, Canada, N2L 3G1*

⁶*Department of Physics & Astronomy, University of Waterloo, Waterloo, Ontario, Canada, N2L 3G1*

⁷*Institute of Theoretical Physics and IQST, Albert-Einstein-Allee 11, Universität Ulm, D-89069 Ulm, Germany*

⁸*IKERBASQUE, Basque Foundation for Science, Maria Diaz de Haro 3, 48013 Bilbao, Spain*

Quantum sensors typically translate external fields into a periodic response whose frequency is then determined by analyses performed in Fourier space. This allows for a linear inference of the parameters that characterize external signals. In practice, however, quantum sensors are able to detect fields only in a narrow range of amplitudes and frequencies. A departure from this range, as well as the presence of significant noise sources and short detection times, lead to a loss of the linear relationship between the response of the sensor and the target field, thus limiting the working regime of the sensor. Here we address these challenges by means of a Bayesian inference approach that is tolerant to strong deviations from desired periodic responses of the sensor and is able to provide reliable estimates even with a very limited number of measurements. We demonstrate our method for an $^{171}\text{Yb}^+$ trapped-ion quantum sensor but stress the general applicability of this approach to different systems.

I. INTRODUCTION

Achieving efficient magnetometry is of considerable importance in a broad range of areas of fundamental and applied science [1, 2]. Nuclear magnetic resonance (NMR) techniques [3, 4], which led to important applications such as NMR spectroscopy [5], magnetic resonance imaging [6], and their recent extensions to the nanoscale [7–9], are specific examples that depend crucially on accurate and efficient magnetometry techniques. Other remarkable applications include magnetic force microscopy [10], which allows the scanning of thin materials for – to throw an example – magnetic recording [11] and may achieve a spatial resolution of the order of tens of nanometers. A new generation of devices that exploit quantum properties to characterize weak electromagnetic signals are superconducting quantum interference devices SQUIDS [12]. These possess excellent magnetic sensitivity and have dimensions ranging from microns [13] to tens of nanometers in the case of nano-SQUIDS [14]. In this spirit, atomic-size sensors such as $^{171}\text{Yb}^+$ [15–17] and $^{40}\text{Ca}^+$ [18] trapped ions, or nitrogen vacancy centers in diamond [19–21] achieve ultimate size-limits for quantum sensors.

Especially interesting is the case of quantum sensors based on $^{171}\text{Yb}^+$ ions that we use as a testbed for our protocol. This ion species encodes the degrees of freedom of the sensor in its $^2S_{\frac{1}{2}}$ spin manifold whose hyperfine levels present a negligible spontaneous emission rate [22]. The latter makes the $^{171}\text{Yb}^+$ ion an ideal atomic-size quantum sensor if properly stabilized against decoherence using dynamical decoupling (DD) methods [23–35]. In particular, owing to its resilience against environmental errors and amplitude fluctuations on the microwave (MW) control, the DD scheme leading to the *dressed state qubit* has been used for quantum information processing [15, 17] and quantum sensing [16]. Despite this robustness and in close similarity with other sensing techniques, the dressed state qubit approach is restricted to a narrow range in

the amplitudes and frequencies of the target electromagnetic signals. A departure from this regime significantly distorts the sensor response and thus makes impossible a direct linear inference of the external field parameters via, e.g., standard fast Fourier transform (FFT) methods.

In this article, we present a method that combines DD techniques to stabilize the quantum sensor with Bayesian inference schemes [36, 37], which enables the accurate estimation of external field parameters from a complex sensor response. This results in a versatile quantum sensing strategy that permits the reconstruction of electromagnetic signals in a wide parameter range, with a minimal previous knowledge of the signal features, and in realistic scenarios involving noise over the sensor and a low number of measurements. As an example, we consider a $^{171}\text{Yb}^+$ ion and demonstrate that Bayesian inference shows a superior performance over standard analysis techniques, such as FFT and least-squares fits. We stress that our method can be adapted to other atomic-size sensors such as $^{40}\text{Ca}^+$ trapped ions or nitrogen vacancy centers in diamond.

II. QUANTUM SENSOR

We start describing the main features of our quantum sensor device. The $^2S_{\frac{1}{2}}$ manifold of the $^{171}\text{Yb}^+$ ion comprises four hyperfine levels named $|0\rangle, |\acute{0}\rangle, |1\rangle,$ and $|-1\rangle$. In an external static magnetic field B_z , the degeneracy of the $|\acute{0}\rangle, |1\rangle, |-1\rangle$ spin levels is removed leading to the diagonal Hamiltonian $H_0 = \omega_0|\acute{0}\rangle\langle\acute{0}| + \sum_{j=-1}^1 \omega_j|j\rangle\langle j|$, with $\omega_{\pm 1} = \frac{A}{4} \pm (\gamma_e - \gamma_n) \frac{B_z}{2}$, and $\omega_0 = -\omega_0 - A/2 = -\frac{3A}{4} - \frac{(\gamma_e + \gamma_n)^2}{4A} B_z^2$, where $A = (2\pi) \times 12.643$ GHz [22] and $\gamma_{e/n}$ is the electronic/nuclear gyromagnetic ratio. We refer to the Supplemental Material (SM) presented in Ref. [38], which includes Refs. [39, 40], for a detailed derivation of H_0 and its spectrum. Under a set of control MW driv-

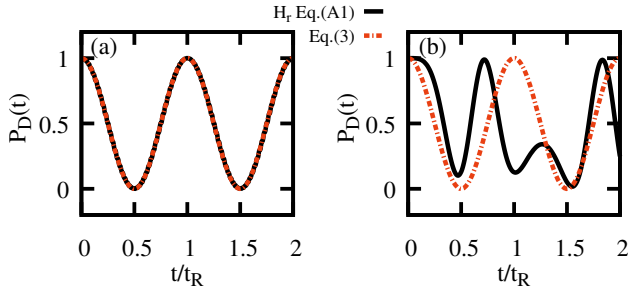


FIG. 1. Dynamical behavior of the population $P_D(t)$ with $P_D(0) = 1$, $\Omega = 2\pi \times 37.27$ kHz as in [16], and when interacting with a rf-signal with (a) $\Omega_{\text{tg}} = 2\pi \times 1$ kHz, $\omega_{\text{tg}} = 2\pi \times 14$ MHz ($B_z = 1$ mT), and $\xi = 0$, or (b) $\Omega_{\text{tg}} = 2\pi \times 8$ kHz, $\omega_{\text{tg}} = 2\pi \times 5.6$ MHz ($B_z = 0.4$ mT) with $\xi = 2\pi \times 0.25$ kHz. The solid (black) line corresponds to the realistic signal, obtained using H_r from Eq. (S18), while dashed (red) is obtained upon various approximations as shown in Eq. (3) with $t_R = 2\pi \sqrt{2}/\Omega_{\text{tg}}$. Note the significant deviations with respect to the Rabi oscillations in (b).

ings, the $^{171}\text{Yb}^+$ ion Hamiltonian reads

$$H = H_0 + \mu(t) (|1\rangle\langle 1| - |-1\rangle\langle -1|) + \sum_j \tilde{\Omega}_j [|1\rangle\langle 0| - |1\rangle\langle 0| + |\dot{0}\rangle\langle -1| + |0\rangle\langle -1| + \text{H.c.}], \quad (1)$$

where $\tilde{\Omega}_j = \Omega_j \cos(\omega_j t + \phi_j)$ denotes the frequency ω_j , phase ϕ_j and Rabi frequency Ω_j of the j th MW driving, and $\mu(t)$ accounts for fluctuations leading to loss of quantum coherence on the magnetically sensitive levels $|1\rangle$ and $|-1\rangle$ [38].

A. Refined atomic-size sensor

To stabilize the quantum sensor, one has to remove the impact of magnetic field fluctuations from the dynamics, i.e., the term $\mu(t) (|1\rangle\langle 1| - |-1\rangle\langle -1|)$ in Eq. (S21). To this end, we tune one of the MW controls in resonance with the $|0\rangle \leftrightarrow |1\rangle$ hyperfine transition, while the other MW-control resonates with $|0\rangle \leftrightarrow |-1\rangle$. Now, a target electromagnetic field (or signal) can be detected by using either the transition $|\dot{0}\rangle \leftrightarrow |1\rangle$ or $|\dot{0}\rangle \leftrightarrow |-1\rangle$. Note that a target signal induces the term $\Omega_{\text{tg}} \cos(\omega_{\text{tg}} t + \phi_{\text{tg}}) [|1\rangle\langle \dot{0}| - |1\rangle\langle 0| + |\dot{0}\rangle\langle -1| + |0\rangle\langle -1| + \text{H.c.}]$ in Eq. (S21).

The standard procedure to estimate Ω_{tg} is illustrated in Ref. [16]. This assumes the target field to be on resonance with the $|\dot{0}\rangle \leftrightarrow |1\rangle$ transition (that is, $\omega_{\text{tg}} = \omega_1 - \omega_0$) leading to $H = -\frac{\mu(t)}{\sqrt{2}} (|D\rangle\langle u| + |D\rangle\langle d| + \text{H.c.}) + \frac{\Omega_{\text{tg}}}{\sqrt{2}} (|u\rangle\langle u| - |d\rangle\langle d|) + \frac{\Omega_{\text{tg}}}{4} (|u\rangle\langle \dot{0}| + |d\rangle\langle \dot{0}| - \sqrt{2}|D\rangle\langle \dot{0}| + \text{H.c.})$ [38]. The new basis $\{|u\rangle, |d\rangle, |D\rangle, |\dot{0}\rangle\}$ is $|u\rangle = \frac{1}{\sqrt{2}}(|B\rangle + |0\rangle)$, $|d\rangle = \frac{1}{\sqrt{2}}(|B\rangle - |0\rangle)$, $|D\rangle = \frac{1}{\sqrt{2}}(|-1\rangle - |1\rangle)$, $|\dot{0}\rangle = |\dot{0}\rangle$, with $|B\rangle = \frac{1}{\sqrt{2}}(|1\rangle + |-1\rangle)$ [15–17]. The noisy term $-\frac{\mu(t)}{\sqrt{2}} (|D\rangle\langle u| + |D\rangle\langle d| + \text{H.c.})$ can be removed since, in the rotating frame defined by the operator $\frac{\Omega_{\text{tg}}}{\sqrt{2}} (|u\rangle\langle u| - |d\rangle\langle d|)$, it rotates at a speed $\propto \Omega$ which allows one to apply the rotating wave approximation (RWA). Analogously,

the terms $-\frac{\mu(t)}{\sqrt{2}} (|D\rangle\langle u| + |D\rangle\langle d| + \text{H.c.})$ and $\frac{\Omega_{\text{tg}}}{4} (|u\rangle\langle \dot{0}| + |d\rangle\langle \dot{0}| + \text{H.c.})$ average out by invoking the RWA if $\Omega_{\text{tg}} \ll \Omega$. One thus finds

$$H = -\frac{\Omega_{\text{tg}}}{2\sqrt{2}} (|D\rangle\langle \dot{0}| + |\dot{0}\rangle\langle D|). \quad (2)$$

Eq. (2) induces Rabi oscillations between $|D\rangle$ and $|\dot{0}\rangle$ at a rate $\propto \Omega_{\text{tg}}$. This allows one to find the amplitude of the electromagnetic signal Ω_{tg} by monitoring, e.g., the population $P_D(t)$ of state $|D\rangle$ at a time t . In particular, from Eq. (2) and for $P_D(0) = 1$, one finds

$$P_D(t) = \cos^2(\pi t/t_R), \quad (3)$$

with $t_R = 2\pi \sqrt{2}/\Omega_{\text{tg}}$. An example of this purely oscillatory response of the sensor is in Fig. 1(a). However, a departure from the regime leading to Eq. (2) induces significant deviations w.r.t. the periodic behavior predicted by Eq. (3). An example of such deviations is given in Fig. 1(b). As we will see later, this challenges the estimation of Ω_{tg} .

A rigorous treatment of the Hamiltonian in Eq. (S21) leads to a more involved expression. The resulting Hamiltonian is denoted by H_r and reproduced in the Appendix for completeness, Eq. (S18), while we refer to [38] for further details in the derivation of Eq. (S18). The Hamiltonian H_r is our refined model that describes the quantum sensor dynamics in a wide parameter regime. In particular, H_r exhibits a non-trivial dependence on Ω_{tg} , as well as on the detuning ξ of the signal w.r.t. the resonant condition, i.e. $\omega_{\text{tg}} = \omega_1 - \omega_0 + \xi$. Contrary to Eq. (2), H_r does not allow us to find analytical expressions for the dynamics of observables such as $P_D(t)$, [cf. Eq. (3)]. However, as we demonstrate later, a specific use of Bayesian methods permits an accurate estimation of target signals in the wide parameter regime described by H_r that surpass the performance of standard techniques such as FFT or least-squares methods.

Regarding the noise sources included in H_r , we have verified that their effect on the sensor dynamics during the time scales considered in this work is negligible. In this respect, one should note that the scheme in H_r includes two MW drivings that eliminate the noise effects induced by, firstly, $\mu(t)$ and, secondly, by Rabi frequency fluctuations. A specific assessment on this – including noise sources taken from Ref. [16] – can be found in [38] which includes Refs. [41–45].

In order to simulate an experimental acquisition of data, we proceed as follows: The data, denoted by \mathbf{D} , is generated by computing the evolution of the quantum sensor state with Hamiltonian H_r at different times t_k with $k = 1, \dots, N_p$. The set \mathbf{D} contains the string of N_m binary outcomes $x_{n;k} \in \{0, 1\}$ for each time instant t_k with $n = 1, \dots, N_m$, that is, $x_{n;k}$ are random variables drawn from a Bernoulli distribution $B(P_k)$ where the success probability P_k is obtained from the dynamics of Hamiltonian H_r . We denote by $X_k = \sum_{n=1}^{N_m} x_{n;k}$ the number of successes recorded at time t_k , so that $P_k^s = X_k/N_m$ is the estimation of P_k from \mathbf{D} . In particular, we initialize the system in the state $|D\rangle$ at time $t = 0$, and compute the probability P_k of finding it in $|D\rangle$ at time t_k , from where the values $x_{n;k}$ are obtained.

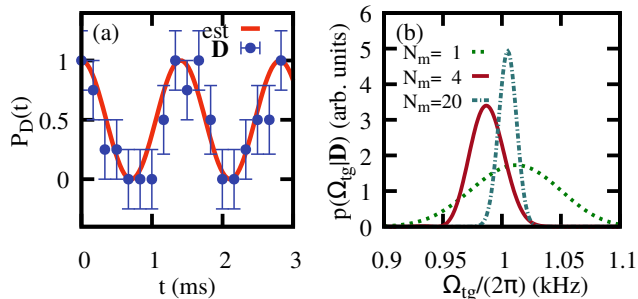


FIG. 2. (a) Simulated $N_p = 18$ observed populations $P_k^s(t_k) = X_k/N_m$ with $N_m = 4$ measurements per point, (points) with error bars indicating a standard deviation due to shot noise [38], together with the reconstructed signal (line) using Bayesian inference for a single unknown parameter Ω_{tg} . (b) Posterior probability distributions for the data in (a) (solid red line) and for the same parameters but $N_m = 1$ (dotted green) and $N_m = 20$ (dashed blue). See main text for the values of $\Omega_{\text{tg}}^{\text{est}}$, and Fig. 1(a) for the rest of parameters.

III. BAYESIAN INFERENCE AND MAGNETOMETRY

In the following, we provide the basics of Bayesian inference as relevant to our method (see for example Refs. [36, 37] for further details). Let us denote by $\Theta = \{\theta_1, \dots, \theta_M\}$ the set of M unknown parameters which we aim to determine using our quantum sensor from the measured data \mathbf{D} . From Bayes' theorem, the probability $p(\Theta|\mathbf{D}) \propto p(\mathbf{D}|\Theta)p(\Theta)$ (typically referred as *posterior*) contains the information we can extract from the data given the prior knowledge $p(\Theta)$, and the likelihood $p(\mathbf{D}|\Theta)$. The observations X_k that form the data \mathbf{D} obey a Bernoulli distribution, i.e. $p(\mathbf{D}|\Theta) = \prod_{k=1}^{N_p} f(X_k, N_m, \tilde{P}_k(t_k; \Theta))$, where $f(x, n, p) = n!/(x!(n-x)!)p^x(1-p)^{n-x}$ accounts for the probability of having recorded exactly x successes from n trials drawn from $B(p)$, while $\tilde{P}_k(t_k; \Theta)$ denotes the expected probability computed using the Hamiltonian H_r , given in Eq. (S18), at time t_k and with parameters Θ . For illustration purposes, we will show the data \mathbf{D} as $P_k^s(t_k)$ together with the shot-noise uncertainties σ_k [38]. It is worth remarking that, while magnetic-field and intensity fluctuations have been taken into account to generate the data \mathbf{D} , their effect is negligible in the considered parameter regime [38]. For the Bayesian inference, the populations $\tilde{P}_k(t_k; \Theta)$ are computed without including these noise sources. Having the posterior distribution, one can obtain the estimated mean and variance value of the unknown parameter θ_j via the marginal distribution $p(\theta_j|\mathbf{D})$, as $\theta_j^{\text{est}} = \int d\theta_j \theta_j p(\theta_j|\mathbf{D})$ and $(\delta\theta_j^{\text{est}})^2 = \int d\theta_j (\theta_j - \theta_j^{\text{est}})^2 p(\theta_j|\mathbf{D})$, respectively, where the marginal reads as $p(\theta_j|\mathbf{D}) = \int \prod_{i \neq j} d\theta_i p(\Theta|\mathbf{D})$.

We exemplify the superior performance of our method over standard analysis techniques with two illustrative cases. For a simplified situation (*Case I*) in which Eq. (3) applies leading to a periodic response, we demonstrate Bayesian inference can handle situations with even single shot measurements providing good estimates. When dealing with more complex signals (*Case II*), we show that Bayesian inference from a few

number of measurements is able to provide reliable estimates where standard analysis techniques are not applicable in general.

A. Case I

In this first scenario, $\Theta = \{\Omega_{\text{tg}}\}$ is the only unknown parameter. Assuming that the RWA can be safely applied and that the target signal is resonant, i.e., $\xi = 0$, the sensor is well approximated by Eq. (2) (cf. Fig. 1(a)) [16]. This allows us to compute the posterior $p(\Omega_{\text{tg}}|\mathbf{D})$ by scanning distinct Ω_{tg} values, from which $\Omega_{\text{tg}}^{\text{est}}$ and $\delta\Omega_{\text{tg}}^{\text{est}}$ can be inferred directly. Here we test our method in the worst case scenario, that is, when no pre-knowledge about the unknown parameter is available. For that, we consider an uninformative prior, i.e., a flat probability distribution, and an observed signal measured at equally spaced time instances t_k separated by Δt , such that $p(\Omega_{\text{tg}}) \propto 1$ for $0 \leq \Omega_{\text{tg}} \leq \Omega_{\text{tg}}^{\text{max}}$, where $\Omega_{\text{tg}}^{\text{max}} = 2\pi/\sqrt{2}\Delta t$. This method can be trivially extended to handle undersampled or unevenly sampled data [38].

We simulate an experimental interrogation of the quantum sensor, recording N_m measurements per each of the N_p different time instances. Since $\Delta t \approx 1/6$ ms, it follows $\Omega_{\text{tg}}^{\text{max}} \approx 2\pi \times 4.2$ kHz. An example is plotted in Fig. 2(a), together with the estimated signal, while the posterior distributions for different observations are illustrated in Fig. 2(b). We obtain very precise estimators even with large shot noise, such as the extreme case of single shots (i.e. $N_m = 1$). In particular, using same parameters than in Fig. 1(a) ($\Omega_{\text{tg}} = 2\pi \times 1$ kHz), we find $\Omega_{\text{tg}}^{\text{est}} = 2\pi \times 1.011(42)$ kHz, $0.988(14)$ kHz and $1.0048(76)$ kHz for three distinct realizations with $N_m = 1, 4$ and 20 measurements, respectively, where the uncertainty is given by $\delta\Omega_{\text{tg}}^{\text{est}}$. See [38] for further details on the precision of the inferred amplitude $\Omega_{\text{tg}}^{\text{est}}$ and the string of outcomes for these realizations. In this simple case and for moderate or large number of measurements, a least-squares fit provide, in average, slightly less accurate results, e.g. $\Omega_{\text{tg}}^{\text{est}} = 2\pi \times 0.947(20)$ kHz for $N_m = 4$ (see [38] for further realizations and details). As the prior probability distribution is flat, the Bayesian estimators simply correspond to maximum likelihood estimators, which are known to outperform least square fits [46]. In addition, note that an analysis using standard FFT methods leads to worse estimators. In particular, for the case in Fig. 2, one obtains $\Omega_{\text{tg}}^{\text{est}} = 2\pi \times 0.94(12)$ kHz [38], which further demonstrates the suitability of Bayesian inference techniques.

B. Case II

A more realistic situation needs to account for potential non-resonant radiation as well as off-resonant transitions within the quantum sensor. Thus, $\Theta = \{\Omega_{\text{tg}}, \xi\}$ where ξ denotes a detuning w.r.t. the resonant condition, and Eq. (S18) is required (cf. Fig. 1(b)). In addition, Markov chain Monte Carlo (MCMC) methods will be employed to efficiently sample the posterior $p(\Theta|\mathbf{D})$ [36, 47]. For that, we consider independent priors, namely, $p(\Omega_{\text{tg}}, \xi) = p(\Omega_{\text{tg}})p(\xi)$,

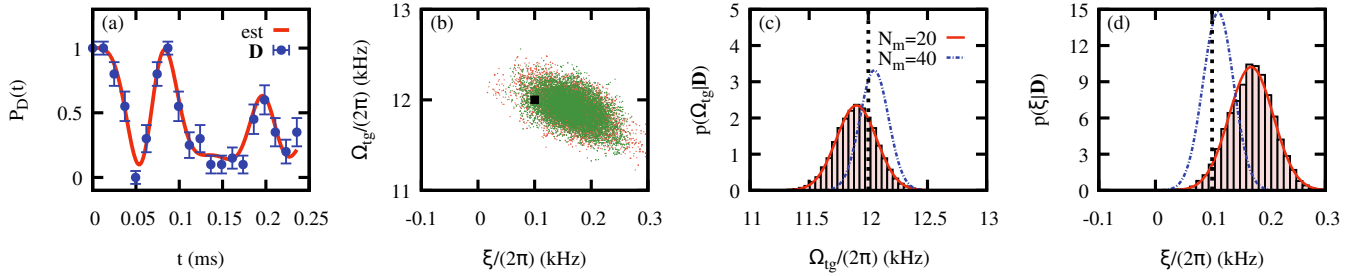


FIG. 3. (a) Simulated observations $P_D(t_k)$ with $N_p = N_m = 20$ (points) together with the reconstructed signal (line) using Bayesian inference and MCMC for Ω_{ig} and ξ unknown. The data \mathbf{D} was generated setting $B_z = 0.5$ mT, with a signal of frequency $\omega_{\text{ig}} \approx 2\pi \times 7$ MHz, with detuning $\xi = 2\pi \times 0.1$ kHz and Rabi frequency $\Omega_{\text{ig}} = 2\pi \times 12$ kHz. (b) Scatter plot of the recorded values Θ_j during the evolution of the MCMC for two independent chains (red and green dots) with $N_{\text{MC}} = 10^4$ but removing the burn-in regime. The ideal value is indicated with a black square. Panels (c) and (d) show the histograms for the marginals $p(\Omega_{\text{ig}}|\mathbf{D})$ and $p(\xi|\mathbf{D})$, respectively, obtained from the MCMC illustrated in (b). The solid red (dashed blue) line corresponds to a Gaussian distribution with equal first and second moments as the marginals for $N_m = 20$ ($N_m = 40$), while the dotted black line indicates the ideal value. The estimated values for the case plotted in (a) are $\Omega_{\text{ig}}^{\text{est}} = 2\pi \times 11.90(17)$ kHz and $\xi^{\text{est}} = 2\pi \times 0.169(39)$ kHz.

taking again $p(\Omega_{\text{ig}})$ completely uninformative in the region $0 \leq \Omega_{\text{ig}} \leq 2\pi \times 50$ kHz, while $p(\xi) = \mathcal{N}(0, \sigma_\xi^2)$ with $\sigma_\xi = 2\pi \times 0.25$ kHz, as we expect close to resonant rf-fields. By randomly choosing an initial point Θ_0 from the prior, we rely on a standard Metropolis algorithm to sample the posterior [47]. After j steps, the proposed point Θ_{j+1} obtained from $\mathcal{N}(\Theta_j, \tilde{\sigma}_p^2)$ where $\tilde{\sigma}_p^2 = \{\tilde{\sigma}_\Omega^2, \tilde{\sigma}_\xi^2\}$ refers to the variance in the proposal distributions, is accepted with probability $\alpha = \min(1, p(\Theta_{j+1}|\mathbf{D})/p(\Theta_j|\mathbf{D}))$. After a sufficient number of steps, $N_{\text{MC}} \gg 1$, the recorded Θ values provide an accurate sampling of $p(\Theta|\mathbf{D})$ and the marginals can be easily computed. Convergence of the MCMC can be checked by the mixing of different Markov chains [38, 47]. Although we illustrate the working method for this case of study with a single example, we stress that the following procedure is general and can be applied to different situations.

In Fig. 3 we have considered a set of data \mathbf{D} obtained for a rf-signal with $\omega_{\text{ig}} \approx 2\pi \times 7$ MHz ($B_z = 0.5$ mT), a detuning of $\xi = 2\pi \times 0.1$ kHz and amplitude $\Omega_{\text{ig}} = 2\pi \times 12$ kHz, and $\Omega = 2\pi \times 37.27$ kHz that protects the sensor against magnetic-field fluctuations, while the data has been generated with $N_p = N_m = 20$ (cf. Figs. 3(a)). For the MCMC we observe that $\tilde{\sigma}_\Omega = 10\tilde{\sigma}_\xi = 2\pi \times 0.1$ kHz yields a good mixing (cf. Fig. 3(b) and [38]), so that the effective size of the MCMC (number of accepted points) amounts approximately to $N_{\text{MC}}/2$ (cf. Fig. 3(b)). We remove the first 200 steps to avoid the burn-in regime [36, 47]. In Figs. 3(c) and (d) we show the marginals $p(\Omega_{\text{ig}}|\mathbf{D})$ and $p(\xi|\mathbf{D})$, respectively, obtained upon $N_{\text{MC}} = 10^4$ steps for five independent Markov chains, which lead to $\Omega_{\text{ig}}^{\text{est}} = 2\pi \times 11.90(17)$ kHz and $\xi^{\text{est}} = 2\pi \times 0.169(39)$ kHz, very close to the ideal values.

The complex and non-harmonic response of the sensor challenges the determination of the unknown parameters for single shot acquisitions [38]. However, for a reduced number of measurements per point, e.g. $N_m = 4$, we still find good estimates for the amplitude $\Omega_{\text{ig}}^{\text{est}} = 2\pi \times 12.91(44)$ kHz, although the data may be better explained under distinct detunings, $\xi^{\text{est}} = 2\pi \times -0.112(90)$ kHz. In a similar manner, by reducing

the shot-noise, more accurate estimates can be obtained, e.g. $\Omega_{\text{ig}}^{\text{est}} = 2\pi \times 12.05(12)$ kHz and $\xi^{\text{est}} = 2\pi \times 0.111(27)$ kHz for $N_m = 40$ measurements per point (cf. Figs. 3(c) and (d)). We provide the string of outcomes \mathbf{D} for each of the realizations and more examples in [38]. Finally, it is worth mentioning that neither least-squares nor FFT techniques are useful in this case due to the complex signal structure. As illustrated in [38], a non-linear least-squares fit to the dynamics dictated by H_r is unable to find suitable parameters unless initialized close to the ideal values and unsuitable to tackle more complex cases such as in bi-modal posterior distributions [38], while at the same time FFT methods exhibit an intricate frequency spectrum of the data \mathbf{D} hindering the identification of the unknown parameters.

IV. CONCLUSIONS

We presented a protocol relying on Bayesian methods that enhance significantly the performance of quantum sensors in realistic scenarios. In particular, we have demonstrated that a quantum sensor can be used even when the character of target signals, as well as the presence of noise and a reduced number of measurements, spoil its ideal functioning leading to strong deviations of the sensor from a simple harmonic response. We illustrate this scheme using a $^{171}\text{Yb}^+$ trapped-ion, and relying on standard MCMC methods if so required by the parameter regime. Our results showcase the suitability of Bayesian inference with respect to standard analysis techniques for parameter estimation. Our method therefore paves the way to use quantum sensors under realistic conditions, significantly extending their working region and reducing the detection times, thus enhancing their adaptability to different scenarios.

ACKNOWLEDGMENTS

We thank Benjamin D’Anjou for helpful comments, and acknowledge financial support from Spanish Government via PGC2018-095113-B-I00 (MCIU/AEI/FEDER, UE), Basque Government via IT986-16, as well as from QMiCS (820505) and OpenSuperQ (820363) of the EU Flagship on Quantum Technologies, and the EU FET Open Grant Quomorphic. J.C. acknowledges the Ramón y Cajal program (RYC2018-025197-I) and support from the UPV/EHU through the grant EHUroPE. M. B. P. acknowledges support by the ERC Synergy Grant HyperQ, the EU Flagship project AsteriQs and the BMBF projects Nanospin and DiaPol. J. F. H. ac-

knowledges support by the Alexander von Humboldt Foundation in form of a Feodor-Lynen Fellowship. R. P. and M. P. acknowledge the support by the SFI-DfE Investigator Programme (grant 15/IA/2864). M. P. acknowledges the H2020 Collaborative Project TEQ (Grant Agreement 766900), the Leverhulme Trust Research Project Grant UltraQuTe (grant RGP-2018-266), the Royal Society Wolfson Fellowship (RSWF/R3/183013) and the UK EPSRC (grant EP/T028106/1).

APPENDIX A: Refined model for the atomic-size sensor

A more rigorous treatment of the Hamiltonian given in Eq. (S21) can be written in the basis $\{|u\rangle, |d\rangle, |D\rangle, |\dot{0}\rangle\}$ as

$$\begin{aligned}
 H_r = & \frac{-\mu(t)}{\sqrt{2}}(|D\rangle\langle u| + |D\rangle\langle d| + \text{H.c.}) + \frac{\Omega}{\sqrt{2}}(|u\rangle\langle u| - |d\rangle\langle d|) - \left[\frac{\Omega}{2\sqrt{2}}(|u\rangle\langle u| - |d\rangle\langle d|) + \frac{\Omega}{4}(|u\rangle\langle D| + |D\rangle\langle d|) \right. \\
 & \left. - \frac{\Omega}{4}(|D\rangle\langle u| + |d\rangle\langle D|) \right] e^{i\gamma_e B_z t} + \left[\frac{\Omega_{\text{tg}}}{4}(|u\rangle\langle \dot{0}| + |d\rangle\langle \dot{0}|) - \frac{\Omega_{\text{tg}}}{2\sqrt{2}}|D\rangle\langle \dot{0}| \right] e^{-i\xi t} + \text{H.c.} \\
 & + \frac{\Omega_{\text{tg}}}{2} \left(\frac{1}{2}|u\rangle\langle \dot{0}| + \frac{1}{2}|d\rangle\langle \dot{0}| - \frac{1}{\sqrt{2}}|D\rangle\langle \dot{0}| \right) e^{2i(\frac{\gamma_e B_z}{2} - \frac{\gamma_e^2 B_z^2}{4A} B_z^2)t} e^{i\xi t} + \frac{\Omega_{\text{tg}}}{2} \left(\frac{1}{2}|\dot{0}\rangle\langle u| + \frac{1}{2}|\dot{0}\rangle\langle d| + \frac{1}{\sqrt{2}}|\dot{0}\rangle\langle D| \right) e^{i\gamma_e B_z t} e^{i\xi t} + \text{H.c.} \\
 & + \frac{\Omega_{\text{tg}}}{2} \left(\frac{1}{2}|\dot{0}\rangle\langle u| + \frac{1}{2}|\dot{0}\rangle\langle d| + \frac{1}{\sqrt{2}}|\dot{0}\rangle\langle D| \right) e^{i\frac{\gamma_e^2}{2A} B_z^2 t} e^{-i\xi t} + \text{H.c.}
 \end{aligned} \tag{A1}$$

where the first term accounts for magnetic-field fluctuations in the states $|D\rangle$ and $|u\rangle$. The rest of the terms appear due to both, a non-resonant target signal $\omega_{\text{tg}} = \omega_1 - \omega_0 + \xi$ with a detuning ξ , as well as a large Rabi frequency Ω_{tg} compared to

the frequency ω_{tg} of the rf-signal. The previous Hamiltonian includes two MW controls with amplitudes Ω . See [38] for the details of the derivation.

-
- [1] J. Lenz, and A. Edelstein, Magnetic sensors and their applications, *IEEE Sensors Journal* **6**, 631 (2006).
- [2] A. Edelstein, Advances in magnetometry, *J. Phys.: Condens. Matter* **19**, 165217 (2007).
- [3] M. H. Levitt, *Spin Dynamics: Basics of Nuclear Magnetic Resonance* (Wiley, West Sussex, 2008).
- [4] R. R. Ernst, G. Bodenhausen, and A. Wokaun, *Principles of Nuclear Magnetic Resonance in One and Two Dimensions* (Oxford Science Publications, 1987).
- [5] H. Günter, *NMR Spectroscopy: Basic Principles, Concepts and Applications in Chemistry* (Wiley, 2013).
- [6] D. B. Plewes, and W. Kucharczyk, Physics of MRI: a primer, *J. Magn. Reson. Imaging* **35**, 1038 (2012).
- [7] C. Müller, X. Kong, J.-M. Cai, K. Melentijevic, A. Stacey, M. Markham, J. Isoya, S. Pezzagna, J. Meijer, J. Du, M. B. Plenio, B. Naydenov, L.P. McGuinness and F. Jelezko, Nuclear magnetic resonance spectroscopy with single spin sensitivity, *Nat. Commun.* **5**, 4703 (2014).
- [8] S. Schmitt, T. Gefen, F. M. Stürner, T. Unden, G. Wolff, Ch. Müller, J. Scheuer, B. Naydenov, M. Markham, S. Pezzagna, J. Meijer, I. Schwarz, M. B. Plenio, A. Retzker, L. P. McGuinness, and F. Jelezko, Submillihertz magnetic spectroscopy performed with a nanoscale quantum sensor, *Science* **356**, 832 (2017).
- [9] I. Schwartz, J. Rosskopf, S. Schmitt, B. Tratzmiller, Q. Chen, L.P. McGuinness, F. Jelezko, and M. B. Plenio, Blueprint for nanoscale NMR, *Sci. Rep.* **9**, 6938 (2019).
- [10] O. Kazakova, R. Puttock, C. Barton, H. Corte-León, M. Jaafar, V. Neu, and A. Asenjo, Frontiers of magnetic force microscopy, *J. Appl. Phys.* **125**, 060901 (2019).
- [11] J. Bai, H. Takahoshi, H. Ito, H. Saito, and S. Ishio, Dot-by-dot analysis of magnetization reversal in perpendicular patterned CoCrPt medium by using magnetic force microscopy, *J. Appl. Phys.* **96**, 1133 (2004).
- [12] R. C. Jaklevic, John Lambe, A. H. Silver, and J. E. Mercereau, Quantum Interference Effects in Josephson Tunneling, *Phys. Rev. Lett.* **12**, 159 (1964).
- [13] J-P. Cleuziou, W. Wernsdorfer, V. Bouchiat, T. Ondarçuhu, and M. Monthieux, Nature, Carbon nanotube superconducting quantum interference device, *Nanotech.* **1**, 53 (2006).
- [14] D. Vasyukov, Y. Anahory, L. Embon, D. Halbertal, J. Cuppens, L. Neeman, A. Finkler, Y. Segev, Y. Myasoedov, M. L. Rappaport, M. E. Huber, and E. Zeldov, A scanning superconducting quantum interference device with single electron spin sensitivity, *Nature Nanotech.* **8**, 639 (2013).

- [15] N. Timoney, I. Baumgart, M. Johanning, A. F. Varón, M. B. Plenio, A. Retzker, and Ch. Wunderlich, Quantum gates and memory using microwave-dressed states, *Nature* **476**, 185 (2011).
- [16] I. Baumgart, J.-M. Cai, A. Retzker, M. B. Plenio, and Ch. Wunderlich, Ultrasensitive Magnetometer using a Single Atom, *Phys. Rev. Lett.* **116**, 240801 (2016).
- [17] S. Weidt, J. Randall, S. C. Webster, K. Lake, A. E. Webb, I. Cohen, T. Navickas, B. Lekitsch, A. Retzker, and W. K. Hensinger, Trapped-Ion Quantum Logic with Global Radiation Fields, *Phys. Rev. Lett.* **117**, 220501 (2016).
- [18] T. Ruster, H. Kaufmann, M. A. Luda, V. Kaushal, C. T. Schmiegelow, F. Schmidt-Kaler, and U. G. Poschinger, Entanglement-Based dc Magnetometry with Separated Ions, *Phys. Rev. X* **7**, 031050 (2017).
- [19] Y. Wu, F. Jelezko, M. B. Plenio, and T. Weil, Diamond Quantum Devices in Biology, *Angew. Chem. Intl. Ed.* **55**, 6586 (2016).
- [20] R. Santagati, A. A. Gentile, S. Knauer, S. Schmitt, S. Paesani, C. Granade, N. Wiebe, C. Osterkamp, L. P. McGuinness, J. Wang, M. G. Thompson, J. G. Rarity, F. Jelezko, and A. Laing, Magnetic-Field Learning Using a Single Electronic Spin in Diamond with One-Photon Readout at Room Temperature, *Phys. Rev. X* **9**, 021019 (2019).
- [21] J. F. Haase, P. J. Vetter, T. Uden, A. Smirne, J. Roskopf, B. Naydenov, A. Stacey, F. Jelezko, M. B. Plenio, and S. F. Huelga, Controllable Non-Markovianity for a Spin Qubit in Diamond, *Phys. Rev. Lett.* **121**, 060401 (2018).
- [22] S. Olmschenk, K. C. Younge, D. L. Moehring, D. N. Matsukevich, P. Maunz, and C. Monroe, Manipulation and detection of a trapped Yb^+ hyperfine qubit, *Phys. Rev. A* **76**, 052314 (2007).
- [23] A. M. Souza, G. A. Álvarez, and D. Suter, Robust dynamical decoupling, *Phil. Trans. R. Soc. A* **370**, 4748 (2012).
- [24] M. J. Biercuk, H. Uys, A. P. VanDevender, N. Shiga, W. M. Itano, and J. J. Bollinger, Optimized dynamical decoupling in a model quantum memory, *Nature* **458**, 996 (2009).
- [25] S. Kotler, N. Akerman, Y. Glickman, A. Keselman, and R. Ozeri, Single-ion quantum lock-in amplifier, *Nature* **473**, 61 (2011).
- [26] J. Casanova, Z.-Y. Wang, J. F. Haase, and M. B. Plenio, Robust dynamical decoupling sequences for individual-nuclear-spin addressing, *Phys. Rev. A* **92**, 042304 (2015).
- [27] R. Puebla, J. Casanova, and M. B. Plenio, A robust scheme for the implementation of the quantum Rabi model in trapped ions, *New J. Phys.* **18**, 113039 (2016).
- [28] R. Puebla, M.-J. Hwang, J. Casanova, and M. B. Plenio, Protected ultrastrong coupling regime of the two-photon quantum Rabi model with trapped ions, *Phys. Rev. A* **95**, 063844 (2017).
- [29] I. Arrazola, J. Casanova, J. S. Pedernales, Z.-Y. Wang, E. Solano, and M. B. Plenio, Pulsed dynamical decoupling for fast and robust two-qubit gates on trapped ions, *Phys. Rev. A* **97**, 052312 (2018).
- [30] I. Arrazola, M. B. Plenio, E. Solano, and J. Casanova, Hybrid Microwave-Radiation Patterns for High-Fidelity Quantum Gates with Trapped Ions, *Phys. Rev. Applied* **13**, 024068 (2020).
- [31] H. J. Mamin, M. Kim, M. H. Sherwood, C. T. Rettner, K. Ohno, D. D. Awschalom, and D. Rugar, Nanoscale Nuclear Magnetic Resonance with a Nitrogen-Vacancy Spin Sensor, *Science* **339**, 557 (2013).
- [32] T. Staudacher, F. Shi, S. Pezzagna, J. Meijer, J. Du, C. A. Meriles, F. Reinhard, and J. Wrachtrup, Nuclear Magnetic Resonance Spectroscopy on a (5-Nanometer)³ Sample Volume, *Science* **339**, 561 (2013).
- [33] F. Shi, Q. Zhang, P. Wang, H. Sun, J. Wang, X. Rong, M. Chen, C. Ju, F. Reinhard, H. Chen, J. Wrachtrup, J. Wang, and J. Du, Single-protein spin resonance spectroscopy under ambient conditions, *Science* **347**, 1135 (2015).
- [34] I. Lovchinsky, A. O. Sushkov, E. Urbach, N. P. de Leon, S. Choi, K. De Greve, R. Evans, R. Gertner, E. Bersin, C. Müller, L. McGuinness, F. Jelezko, R. L. Walsworth, H. Park, and M. D. Lukin, Nuclear magnetic resonance detection and spectroscopy of single proteins using quantum logic, *Science* **351**, 836 (2016).
- [35] N. Aslam, M. Pfender, P. Neumann, R. Reuter, A. Zappe, F. F. de Oliveira, A. Denisenko, H. Sumiya, S. Onoda, J. Isoya, and J. Wrachtrup, Nanoscale nuclear magnetic resonance with chemical resolution, *Science* **357**, 67 (2017).
- [36] W. von der Linden, V. Dose, and U. von Toussaint, *Bayesian Probability Theory*, (Cambridge University Press, Cambridge, UK, 2014).
- [37] A. Gelman, J. B. Carlin, and D. B. Rubin, *Bayesian Data Analysis*, 2nd ed. (Chapman&Hall/CRC, 2004).
- [38] See Supplemental Material for further explanations and details of the calculation.
- [39] D. J. Griffiths, *Introduction to Quantum Mechanics* (Prentice Hall, New Jersey, 1994).
- [40] I. Reichenbach, and I. H. Deutsch, Sideband Cooling while Preserving Coherences in the Nuclear Spin State in Group-II-like Atoms, *Phys. Rev. Lett.* **99**, 123001 (2007).
- [41] G. E. Uhlenbeck, and L. S. Ornstein, On the Theory of the Brownian Motion, *Phys. Rev.* **36**, 823 (1930).
- [42] D. T. Gillespie, Exact numerical simulation of the Ornstein-Uhlenbeck process and its integral, *Phys. Rev. E* **54**, 2084 (1996).
- [43] D. T. Gillespie, The mathematics of Brownian motion and Johnson noise, *Am. J. Phys.* **64**, 225 (1996).
- [44] J.-M. Cai, B. Naydenov, R. Pfeiffer, L. P. McGuinness, K. D. Jahnke, F. Jelezko, M. B. Plenio, and A. Retzker, Robust dynamical decoupling with concatenated continuous driving, *New J. Phys.* **14**, 113023 (2012).
- [45] G. Mikelsons, I. Cohen, A. Retzker, and M. B. Plenio, Universal set of gates for microwave dressed-state quantum computing, *New J. Phys.* **17**, 053032 (2015).
- [46] U. Genschel, and W. Q. Meeker, A Comparison of Maximum Likelihood and Median-Rank Regression for Weibull Estimation, *Quality Engineering*, **22**, 236 (2010).
- [47] W. R. Gilks, S. Richardson, and D. J. Spiegelhalter, *Markov Chain Monte Carlo in practice*, (Chapman&Hall/CRC, 1996).

Supplemental Material

Versatile Atomic Magnetometry Assisted by Bayesian Inference

R. Puebla,^{1,2} Y. Ban,^{3,4} J. F. Haase,^{5,6} M. B. Plenio,⁷ M. Paternostro,² and J. Casanova^{3,8}

¹*Instituto de Física Fundamental, IFF-CSIC, Calle Serrano 113b, 28006 Madrid, Spain*

²*Centre for Theoretical Atomic, Molecular, and Optical Physics,*

School of Mathematics and Physics, Queen's University, Belfast BT7 1NN, United Kingdom

³*Department of Physical Chemistry, University of the Basque Country UPV/EHU, Apartado 644, 48080 Bilbao, Spain*

⁴*School of Materials Science and Engineering, Shanghai University, 200444 Shanghai, China*

⁵*Institute for Quantum Computing, University of Waterloo, Waterloo, Ontario, Canada, N2L 3G1*

⁶*Department of Physics & Astronomy, University of Waterloo, Waterloo, Ontario, Canada, N2L 3G1*

⁷*Institute of Theoretical Physics and IQST, Albert-Einstein Allee 11, Universität Ulm, 89069 Ulm, Germany*

⁸*IKERBASQUE, Basque Foundation for Science, Maria Diaz de Haro 3, 48013 Bilbao, Spain*

I. ¹⁷¹Yb⁺ SENSOR ENERGY LEVELS

In this appendix we provide a summary of the ¹⁷¹Yb⁺ physical properties. We are interested in the long-lived $^2S_{\frac{1}{2}}$ manifold of the ¹⁷¹Yb⁺ ion [S1]. This means $L = 0$, i.e. zero angular momentum, and spin $S = \frac{1}{2}$ according to the general spectroscopic notation $^{2S+1}L_J$. The hyperfine interaction in this manifold is created because the ¹⁷¹Yb⁺ nucleus carries a spin $I = \frac{1}{2}$ which interacts with the electronic spin [S1] leading to the following Hamiltonian

$$H = A \mathbf{J} \cdot \mathbf{I}, \quad (\text{S1})$$

where \mathbf{J} is a spin-1/2 operator for the electron (note we are in the $^2S_{\frac{1}{2}}$ manifold), and \mathbf{I} is a nuclear spin-1/2 operator. This means that we can write $\mathbf{I} = \frac{1}{2}\vec{\sigma}_1$ and $\mathbf{J} = \frac{1}{2}\vec{\sigma}_2$ where $\vec{\sigma}_{1,2} = (\sigma_{1,2}^x, \sigma_{1,2}^y, \sigma_{1,2}^z)$. In addition, A is the magnetic hyperfine constant which is $A \approx (2\pi) \times 12.643$ GHz as measured in [S1]. The Hamiltonian that describes this situation once a magnetic field $\vec{B} = B_z \hat{z}$ is included reads

$$H = A \mathbf{J} \cdot \mathbf{I} + g_J \mu_B \mathbf{J} \cdot \vec{B} - g_I \mu_N \mathbf{I} \cdot \vec{B} \quad (\text{S2})$$

where $g_J = \left[1 + (g_S - 1) \frac{j(j+1) - l(l+1) + s(s+1)}{2j(j+1)} \right]$ is the Landé g -factor of the atom (see for example [S2]) and $g_S \approx 2.0023$ is the responsible of the anomalous gyromagnetic factor of the electron spin (in our case $j = s = 1/2$ and $l = 0$, hence $g_J = 1 + (g_S - 1) = g_S$). Note that a similar expression for the 1P_1 subspace can be found in [S3].

The static magnetic field leads to a Zeeman splitting of the energy levels. If we redefine $g_S \mu_B \equiv \hbar \gamma_e$ and $g_I \mu_N \equiv \hbar \gamma_n$, where $\gamma_e = (2\pi) \times 2.8024$ MHz/G and γ_n the gyromagnetic factor of the ¹⁷¹Yb⁺ nucleus, with $\gamma_n \equiv \gamma_{^{171}\text{Yb}^+} = (2\pi) \times 4.7248$ kHz/G, i.e. $\gamma_n \ll \gamma_e$, the Hamiltonian (S2) can be written as

$$H = A \mathbf{J} \cdot \mathbf{I} + \gamma_e B_z J_z - \gamma_n B_z I_z. \quad (\text{S3})$$

In the basis $\{|11\rangle, |10\rangle, |01\rangle, |00\rangle\}$ (with $\sigma_z|1\rangle = |1\rangle$ and $\sigma_z|0\rangle = -|0\rangle$) one can write

$$H = \begin{pmatrix} \frac{A}{4} + (\gamma_e - \gamma_n) \frac{B_z}{2} & 0 & 0 & 0 \\ 0 & -\frac{A}{4} + (\gamma_e + \gamma_n) \frac{B_z}{2} & \frac{A}{2} & 0 \\ 0 & \frac{A}{2} & -\frac{A}{4} - (\gamma_e + \gamma_n) \frac{B_z}{2} & 0 \\ 0 & 0 & 0 & \frac{A}{4} - (\gamma_e - \gamma_n) \frac{B_z}{2} \end{pmatrix}. \quad (\text{S4})$$

The states $|1\rangle = |11\rangle$ and $|-1\rangle = |00\rangle$, have the eigenfrequencies $\omega_1 = \frac{A}{4} + (\gamma_e - \gamma_n) \frac{B_z}{2}$ and $\omega_{-1} = \frac{A}{4} - (\gamma_e - \gamma_n) \frac{B_z}{2}$, while diagonalization of Eq. (S4) leads to two additional energies, namely, $\omega_0 = -\frac{A}{4} + \frac{A}{2} \sqrt{1 + \left[\frac{(\gamma_e + \gamma_n) B_z}{A} \right]^2}$ and $\omega_0 = -\frac{A}{4} - \frac{A}{2} \sqrt{1 + \left[\frac{(\gamma_e + \gamma_n) B_z}{A} \right]^2}$. The latter expressions can be expanded if $\left[\frac{(\gamma_e + \gamma_n) B_z}{A} \right] \ll 1$ (note this is our case since we consider low values for B_z) leading to $\omega_0 \approx \frac{A}{4} + \frac{(\gamma_e + \gamma_n)^2}{4A} B_z^2$ and $\omega_0 \approx -\frac{3A}{4} - \frac{(\gamma_e + \gamma_n)^2}{4A} B_z^2$. The quantity $\omega_0 - \omega_0 = A + \frac{(\gamma_e + \gamma_n)^2}{2A} B_z^2$ where the factor $\frac{(\gamma_e + \gamma_n)^2}{2A} \approx (2\pi) \times 310.8 \frac{\text{Hz}}{\text{G}^2}$ is known as the second-order Zeeman shift [S1].

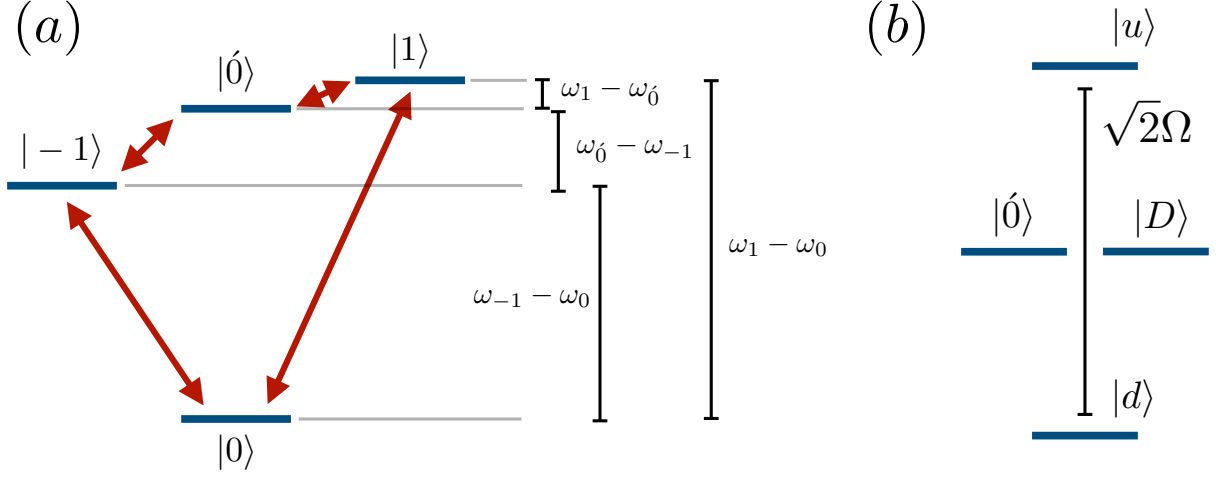


FIG. S1. (a) Energy scheme of the $^{171}\text{Yb}^+$ atom under the presence of a magnetic field according to Eq. (S6) as well as the allowed transitions that appear as a consequence of introducing an external MW field. (b) Dressed state qubit basis and the corresponding energy differences (cf. Eqs. (S27) and (S28)).

As a summary, Hamiltonian (S4) has the following eigenstates and eigenvalues

$$\begin{aligned}
 |1\rangle &= |11\rangle \longrightarrow \omega_1 = \frac{A}{4} + (\gamma_e - \gamma_n) \frac{B_z}{2} \\
 |-1\rangle &= |00\rangle \longrightarrow \omega_{-1} = \frac{A}{4} - (\gamma_e - \gamma_n) \frac{B_z}{2} \\
 |\acute{0}\rangle &= \alpha|10\rangle + \beta|01\rangle \longrightarrow \omega_{\acute{0}} \approx \frac{A}{4} + \frac{(\gamma_e + \gamma_n)^2}{4A} B_z^2 \\
 |0\rangle &= \gamma|10\rangle + \delta|01\rangle \longrightarrow \omega_0 \approx -\frac{3A}{4} - \frac{(\gamma_e + \gamma_n)^2}{4A} B_z^2
 \end{aligned} \tag{S5}$$

where $\alpha = \sqrt{\frac{1}{1 + (\frac{\omega_0 - a}{b})^2}}$, $\beta = \frac{\omega_0 - a}{b} \sqrt{\frac{1}{1 + (\frac{\omega_0 - a}{b})^2}}$, $\gamma = \sqrt{\frac{1}{1 + (\frac{\omega_0 - a}{b})^2}}$, and $\delta = \frac{\omega_0 - a}{b} \sqrt{\frac{1}{1 + (\frac{\omega_0 - a}{b})^2}}$, with $a = -\frac{A}{4} + (\gamma_e + \gamma_n) \frac{B_z}{2}$ and $b = \frac{A}{2}$.

In this new basis the Hamiltonian (S3) can be written as

$$H = \omega_1|1\rangle\langle 1| + \omega_{\acute{0}}|\acute{0}\rangle\langle \acute{0}| + \omega_{-1}|-1\rangle\langle -1| + \omega_0|0\rangle\langle 0|. \tag{S6}$$

In Fig. S1(a) we have sketched the energy diagram of the $^{171}\text{Yb}^+$ ion's $^2S_{\frac{1}{2}}$ manifold. We can induce transitions among the states in the diagonal basis $\{|0\rangle, |-1\rangle, |\acute{0}\rangle, |1\rangle\}$ with radiofrequency and microwave fields. For example, the driving $B_x \cos(\omega t + \phi)$ leads to the following interaction

$$H = A \mathbf{J} \cdot \mathbf{I} + \gamma_e B_z J_z - \gamma_n B_z I_z + \gamma_e B_x J_x \cos(\omega t + \phi) - \gamma_n B_x I_x \cos(\omega t + \phi). \tag{S7}$$

Or, in the diagonal basis

$$H = \omega_1|1\rangle\langle 1| + \omega_{\acute{0}}|\acute{0}\rangle\langle \acute{0}| + \omega_{-1}|-1\rangle\langle -1| + \omega_0|0\rangle\langle 0| + \gamma_e B_x J_x \cos(\omega t + \phi) - \gamma_n B_x I_x \cos(\omega t + \phi). \tag{S8}$$

To see the induced transitions as a consequence of the newly introduced driving field, we have to expand J_x and I_x in the new basis. With the help of the expressions

$$\begin{aligned}
 |10\rangle &= \frac{\delta}{\delta\alpha - \beta\gamma} \left(|\acute{0}\rangle - \frac{\beta}{\delta} |0\rangle \right), \\
 |01\rangle &= \frac{\gamma}{\gamma\beta - \alpha\delta} \left(|\acute{0}\rangle - \frac{\alpha}{\gamma} |0\rangle \right),
 \end{aligned} \tag{S9}$$

one can easily find

$$J_x = \frac{1}{2(\gamma\beta - \alpha\delta)} \left[\gamma|1\rangle\langle \acute{0}| - \alpha|1\rangle\langle 0| - \delta|\acute{0}\rangle\langle -1| + \beta|0\rangle\langle -1| + \text{H.c.} \right], \tag{S10}$$

and

$$I_x = \frac{1}{2(\gamma\beta - \alpha\delta)} \left[-\delta|1\rangle\langle 0| + \beta|1\rangle\langle 0| + \gamma|\acute{0}\rangle\langle -1| - \alpha|\acute{0}\rangle\langle -1| + \text{H.c.} \right]. \quad (\text{S11})$$

In this manner, one can write

$$H = \omega_1|1\rangle\langle 1| + \omega_0|\acute{0}\rangle\langle \acute{0}| + \omega_{-1}|-1\rangle\langle -1| + \omega_0|0\rangle\langle 0| + \frac{B_x}{2} \left[c_{1\acute{0}}|1\rangle\langle \acute{0}| + c_{10}|1\rangle\langle 0| + c_{\acute{0}-1}|\acute{0}\rangle\langle -1| + c_{0-1}|0\rangle\langle -1| + \text{H.c.} \right] \cos(\omega t + \phi) \quad (\text{S12})$$

where

$$\begin{aligned} c_{1\acute{0}} &= \frac{1}{\gamma\beta - \alpha\delta} (\gamma_e\gamma + \gamma_n\delta), \\ c_{10} &= \frac{-1}{\gamma\beta - \alpha\delta} (\gamma_e\alpha + \gamma_n\beta), \\ c_{\acute{0}-1} &= \frac{-1}{\gamma\beta - \alpha\delta} (\gamma_e\delta + \gamma_n\gamma), \\ c_{0-1} &= \frac{1}{\gamma\beta - \alpha\delta} (\gamma_e\beta + \gamma_n\alpha). \end{aligned} \quad (\text{S13})$$

In Hamiltonian (S12) we can see the allowed transitions that would occur when the frequency ω of the external driving is on resonance with the corresponding energy difference of each of the transitions. More specifically, in the rotating frame of $H_0 = \omega_1|1\rangle\langle 1| + \omega_0|\acute{0}\rangle\langle \acute{0}| + \omega_{-1}|-1\rangle\langle -1| + \omega_0|0\rangle\langle 0|$, one can find

$$H = \frac{B_x}{4} \left[c_{1\acute{0}}|1\rangle\langle \acute{0}| e^{i(\omega_1 - \omega_0)t} + c_{10}|1\rangle\langle 0| e^{i(\omega_1 - \omega_0)t} + c_{\acute{0}-1}|\acute{0}\rangle\langle -1| e^{i(\omega_0 - \omega_{-1})t} + c_{0-1}|0\rangle\langle -1| e^{i(\omega_0 - \omega_{-1})t} + \text{H.c.} \right] \left[e^{i(\omega t + \phi)} + e^{-i(\omega t + \phi)} \right]. \quad (\text{S14})$$

The required energy of each transition reads as (in Fig. S1 a) one can see the energy diagram)

$$\begin{aligned} \omega_1 - \omega_0 &\approx \frac{\gamma_e B_z}{2} - \frac{\gamma_e^2}{4A} B_z^2, \\ \omega_1 - \omega_{-1} &\approx A + \frac{\gamma_e B_z}{2} + \frac{\gamma_e^2}{4A} B_z^2, \\ \omega_0 - \omega_{-1} &\approx \frac{\gamma_e B_z}{2} + \frac{\gamma_e^2}{4A} B_z^2, \\ \omega_{-1} - \omega_0 &\approx A - \frac{\gamma_e B_z}{2} + \frac{\gamma_e^2}{4A} B_z^2. \end{aligned} \quad (\text{S15})$$

In addition, when several drivings act on the system, one can straightforwardly extend Hamiltonian (S12) to

$$H = \omega_1|1\rangle\langle 1| + \omega_0|\acute{0}\rangle\langle \acute{0}| + \omega_{-1}|-1\rangle\langle -1| + \omega_0|0\rangle\langle 0| + \sum_j \frac{B_x^j}{2} \left[c_{1\acute{0}}^j|1\rangle\langle \acute{0}| + c_{10}^j|1\rangle\langle 0| + c_{\acute{0}-1}^j|\acute{0}\rangle\langle -1| + c_{0-1}^j|0\rangle\langle -1| + \text{H.c.} \right] \cos(\omega_j t + \phi_j). \quad (\text{S16})$$

In order to complete the model, we have to consider the effect of magnetic-field fluctuations. Hence, we introduce a noise source in ω_1 and ω_{-1} . In this respect, note that the $|0\rangle$ and $|\acute{0}\rangle$ hyperfine levels also fluctuate but with a much more smaller intensity since the magnetic field enters through the small second-order Zeeman shift, cf. Eq. (S5). This leads to

$$H = \omega_1|1\rangle\langle 1| + \omega_0|\acute{0}\rangle\langle \acute{0}| + \omega_{-1}|-1\rangle\langle -1| + \omega_0|0\rangle\langle 0| + \mu(t)(|1\rangle\langle 1| - |-1\rangle\langle -1|) + \sum_j \frac{B_x^j}{2} \left[c_{1\acute{0}}^j|1\rangle\langle \acute{0}| + c_{10}^j|1\rangle\langle 0| + c_{\acute{0}-1}^j|\acute{0}\rangle\langle -1| + c_{0-1}^j|0\rangle\langle -1| + \text{H.c.} \right] \cos(\omega_j t + \phi_j). \quad (\text{S17})$$

Note that the noisy term $\mu(t)(|1\rangle\langle 1| - |-1\rangle\langle -1|)$ can be understood by inspecting the expressions for ω_1 and ω_{-1} and considering that B_z carries a fluctuation such that the static magnetic field equals to $B_z[1 + \xi(t)]$, and $B_z\xi(t)(\gamma_e - \gamma_n)/2 = \mu(t)$.

II. DERIVATION OF EQS. (2) AND (A1) OF MAIN TEXT

Here we provide the details to derive Eqs. (2), and thus (3), and the Hamiltonian H_r given in Eq. (A1) of the main text. In particular, in **Section II A** we find Eq. (2) that describes the effective Hamiltonian used in standard measurements schemes. In **Section II B** we derive Eq. (A1) which is the target Hamiltonian H_r we use in the main text. Equation (A1) is reproduced here for convenience

$$\begin{aligned}
H_r = & \frac{-\mu(t)}{\sqrt{2}}(|D\rangle\langle u| + |D\rangle\langle d| + \text{H.c.}) + \frac{\Omega}{\sqrt{2}}(|u\rangle\langle u| - |d\rangle\langle d|) \\
& - \left[\frac{\Omega}{2\sqrt{2}}(|u\rangle\langle u| - |d\rangle\langle d|) + \frac{\Omega}{4}(|u\rangle\langle D| + |D\rangle\langle d|) - \frac{\Omega}{4}(|D\rangle\langle u| + |d\rangle\langle D|) \right] e^{i\gamma_e B_z t} + \text{H.c.} \\
& + \left[\frac{\Omega_{\text{tg}}}{4}(|u\rangle\langle \acute{o}| + |d\rangle\langle \acute{o}|) - \frac{\Omega_{\text{tg}}}{2\sqrt{2}}|D\rangle\langle \acute{o}| \right] e^{-i\xi t} + \text{H.c.} \\
& + \frac{\Omega_{\text{tg}}}{2} \left(\frac{1}{2}|u\rangle\langle \acute{o}| + \frac{1}{2}|d\rangle\langle \acute{o}| - \frac{1}{\sqrt{2}}|D\rangle\langle \acute{o}| \right) e^{2i(\frac{\gamma_e B_z}{2} - \frac{\gamma_e^2}{4\lambda} B_z^2)t} e^{i\xi t} + \text{H.c.} \\
& + \frac{\Omega_{\text{tg}}}{2} \left(\frac{1}{2}|\acute{o}\rangle\langle u| + \frac{1}{2}|\acute{o}\rangle\langle d| + \frac{1}{\sqrt{2}}|\acute{o}\rangle\langle D| \right) e^{i\gamma_e B_z t} e^{i\xi t} + \text{H.c.} \\
& + \frac{\Omega_{\text{tg}}}{2} \left(\frac{1}{2}|\acute{o}\rangle\langle u| + \frac{1}{2}|\acute{o}\rangle\langle d| + \frac{1}{\sqrt{2}}|\acute{o}\rangle\langle D| \right) e^{i\frac{\gamma_e^2}{2\lambda} B_z^2 t} e^{-i\xi t} + \text{H.c.} \tag{S18}
\end{aligned}$$

For the sake of simplicity in the presentation of the results, we will make the following assumptions: **(i)** Since $\gamma_n \ll \gamma_e$ and $|\alpha|, |\beta|, |\gamma|, |\delta|$ are similar for the values of B_z we consider in the main text, the set of equations (S13) is

$$\begin{aligned}
c_{10} &= \frac{1}{\gamma\beta - \alpha\delta}(\gamma_e\gamma + \gamma_n\delta) \approx \frac{\gamma_e\gamma}{\gamma\beta - \alpha\delta}, \\
c_{10} &= \frac{-1}{\gamma\beta - \alpha\delta}(\gamma_e\alpha + \gamma_n\beta) \approx \frac{-\gamma_e\alpha}{\gamma\beta - \alpha\delta}, \\
c_{\acute{o}-1} &= \frac{-1}{\gamma\beta - \alpha\delta}(\gamma_e\delta + \gamma_n\gamma) \approx \frac{-\gamma_e\delta}{\gamma\beta - \alpha\delta}, \\
c_{0-1} &= \frac{1}{\gamma\beta - \alpha\delta}(\gamma_e\beta + \gamma_n\alpha) \approx \frac{\gamma_e\beta}{\gamma\beta - \alpha\delta}. \tag{S19}
\end{aligned}$$

And **(ii)**, for the parameter regimes used in the main text one can further approximate

$$\begin{aligned}
c_{10} &= \frac{1}{\gamma\beta - \alpha\delta}(\gamma_e\gamma + \gamma_n\delta) \approx \frac{\gamma_e\gamma}{\gamma\beta - \alpha\delta} \approx \frac{1}{\sqrt{2}}\gamma_e, \\
c_{10} &= \frac{-1}{\gamma\beta - \alpha\delta}(\gamma_e\alpha + \gamma_n\beta) \approx \frac{-\gamma_e\alpha}{\gamma\beta - \alpha\delta} \approx \frac{-1}{\sqrt{2}}\gamma_e, \\
c_{\acute{o}-1} &= \frac{-1}{\gamma\beta - \alpha\delta}(\gamma_e\delta + \gamma_n\gamma) \approx \frac{-\gamma_e\delta}{\gamma\beta - \alpha\delta} \approx \frac{1}{\sqrt{2}}\gamma_e, \\
c_{0-1} &= \frac{1}{\gamma\beta - \alpha\delta}(\gamma_e\beta + \gamma_n\alpha) \approx \frac{\gamma_e\beta}{\gamma\beta - \alpha\delta} \approx \frac{1}{\sqrt{2}}\gamma_e. \tag{S20}
\end{aligned}$$

Hence, under **(i)** and **(ii)**, one can write the system Hamiltonian, i.e. Eq. (S17) as

$$\begin{aligned}
H = & \omega_1|1\rangle\langle 1| + \omega_0|\acute{o}\rangle\langle \acute{o}| + \omega_{-1}|-1\rangle\langle -1| + \omega_0|0\rangle\langle 0| + \mu(t) (|1\rangle\langle 1| - |-1\rangle\langle -1|) \\
& + \sum_j \Omega_j \left[|1\rangle\langle \acute{o}| - |1\rangle\langle 0| + |\acute{o}\rangle\langle -1| + |0\rangle\langle -1| + \text{H.c.} \right] \cos(\omega_j t + \phi_j), \tag{S21}
\end{aligned}$$

where $\Omega_j = \frac{B_j \gamma_e}{2\sqrt{2}}$.

II A. Standard measurement scheme

In order to remove magnetic field fluctuations from our sensor one can use two microwave fields resonant with the $0 \leftrightarrow 1$ and $0 \leftrightarrow -1$ hyperfine transitions of the $^{171}\text{Yb}^+$ ion. Note that this is the scheme used in Refs. [S4, S5]. In particular, if one sets $\Omega = \Omega_1 = \Omega_2$, $\phi_1 = \pi$ and $\phi_2 = 0$, the following Hamiltonian is obtained (in the rotating frame of $H_0 = \omega_1|1\rangle\langle 1| + \omega_0|\hat{0}\rangle\langle \hat{0}| + \omega_{-1}|-1\rangle\langle -1| + \omega_0|0\rangle\langle 0|$)

$$H^I = \mu(t)(|1\rangle\langle 1| - |-1\rangle\langle -1|) + \frac{\Omega}{2}(|1\rangle\langle 0| + |-1\rangle\langle 0| + \text{H.c.}). \quad (\text{S22})$$

In order to find the previous equation, one has to neglect terms rotating at a frequency $\propto \gamma_e B_z$ by invoking the rotating wave approximation (RWA).

The next step is to demonstrate how the addition of the two MW drivings leads to the cancellation of $\mu(t)$. For that, it is convenient to define a new basis $\{|u\rangle, |d\rangle, |D\rangle, |\hat{0}\rangle\}$ such that

$$\begin{aligned} |u\rangle &= \frac{1}{\sqrt{2}}(|B\rangle + |0\rangle), \\ |d\rangle &= \frac{1}{\sqrt{2}}(|B\rangle - |0\rangle), \\ |D\rangle &= \frac{1}{\sqrt{2}}(|-1\rangle - |1\rangle), \end{aligned} \quad (\text{S23})$$

and $|B\rangle = \frac{1}{\sqrt{2}}(|1\rangle + |-1\rangle)$. In this new basis, Eq. (S22) becomes

$$H = -\frac{\mu(t)}{\sqrt{2}}(|D\rangle\langle u| + |D\rangle\langle d| + \text{H.c.}) + \frac{\Omega}{\sqrt{2}}(|u\rangle\langle u| - |d\rangle\langle d|). \quad (\text{S24})$$

Now, it is easy to see that, in the rotating frame of $\frac{\Omega}{\sqrt{2}}(|u\rangle\langle u| - |d\rangle\langle d|)$, the noisy term rotates at a speed $\propto \Omega$ and thus it can be eliminated with a suitable Ω .

Let us now consider an additional rf-field signal interacting with the sensor, i.e we add an extra driving to Eq. (S21) whose Rabi frequency (Ω_{tg}) we want to determine. To this end, we use the energy difference between the $|\hat{0}\rangle \leftrightarrow |1\rangle$ and $|\hat{0}\rangle \leftrightarrow |-1\rangle$ transitions. This energy difference is caused by the second-order Zeeman shift which is $\propto \frac{\gamma_e^2}{4A} B_z^2$ and, ideally, it would allow us to only excite the $|\hat{0}\rangle \leftrightarrow |1\rangle$ transition. In this case, the general Hamiltonian is

$$\begin{aligned} H &= \omega_1|1\rangle\langle 1| + \omega_0|\hat{0}\rangle\langle \hat{0}| + \omega_{-1}|-1\rangle\langle -1| + \omega_0|0\rangle\langle 0| + \mu(t)(|1\rangle\langle 1| - |-1\rangle\langle -1|) \\ &+ \sum_j \Omega_j \left[|1\rangle\langle \hat{0}| - |1\rangle\langle 0| + |\hat{0}\rangle\langle -1| + |0\rangle\langle -1| + \text{H.c.} \right] \cos(\omega_j t + \phi_j) \\ &+ \Omega_{\text{tg}} \left[|1\rangle\langle \hat{0}| - |1\rangle\langle 0| + |\hat{0}\rangle\langle -1| + |0\rangle\langle -1| + \text{H.c.} \right] \cos(\omega_{\text{tg}} t + \phi_{\text{tg}}). \end{aligned} \quad (\text{S25})$$

In the rotating frame of $H_0 = \omega_1|1\rangle\langle 1| + \omega_0|\hat{0}\rangle\langle \hat{0}| + \omega_{-1}|-1\rangle\langle -1| + \omega_0|0\rangle\langle 0|$ and selecting again $\Omega = \Omega_1 = \Omega_2$, $\phi_1 = \pi$ and $\phi_2 = 0$ one can find that the previous Hamiltonian becomes

$$\begin{aligned} H &= -\frac{\mu(t)}{\sqrt{2}}(|D\rangle\langle u| + |D\rangle\langle d| + \text{H.c.}) + \frac{\Omega}{\sqrt{2}}(|u\rangle\langle u| - |d\rangle\langle d|) \\ &+ \Omega_{\text{tg}} \left[|1\rangle\langle \hat{0}| e^{i(\omega_1 - \omega_0)t} - |1\rangle\langle 0| e^{i(\omega_1 - \omega_0)t} + |\hat{0}\rangle\langle -1| e^{i(\omega_0 - \omega_{-1})t} + |0\rangle\langle -1| e^{i(\omega_0 - \omega_{-1})t} + \text{H.c.} \right] \cos(\omega_{\text{tg}} t + \phi_{\text{tg}}). \end{aligned} \quad (\text{S26})$$

If we tune $\omega_{\text{tg}} = \omega_1 - \omega_0$ and $\phi_{\text{rf}} = 0$ in Eq. (S26), and assuming that oscillating terms can be eliminated by the RWA, we would find (note we have selected $\phi_{\text{tg}} = 0$, but similar result can be derived for an arbitrary value of ϕ_{tg})

$$H = -\frac{\mu(t)}{\sqrt{2}}(|D\rangle\langle u| + |D\rangle\langle d| + \text{H.c.}) + \frac{\Omega}{\sqrt{2}}(|u\rangle\langle u| - |d\rangle\langle d|) + \frac{\Omega_{\text{tg}}}{4}(|u\rangle\langle \hat{0}| + |d\rangle\langle \hat{0}| + \text{H.c.}) - \frac{\Omega_{\text{tg}}}{2\sqrt{2}}(|D\rangle\langle \hat{0}| + |\hat{0}\rangle\langle D|), \quad (\text{S27})$$

which, in the rotating frame of $\frac{\Omega}{\sqrt{2}}(|u\rangle\langle u| - |d\rangle\langle d|)$, it adopts the following form

$$H = -\frac{\Omega_{\text{tg}}}{2\sqrt{2}}(|D\rangle\langle \hat{0}| + |\hat{0}\rangle\langle D|). \quad (\text{S28})$$

Hamiltonian (S28) corresponds to the Eq. (2) given in the main text, from where it follows Eq. (3). Recall that this is the approach followed in Ref. [S6].

II B. Refined measurement scheme

The previous scheme assumes several approximations that rely on the energy difference among the $|\pm 1\rangle$ and $|\acute{0}\rangle$ states, and among $|\pm 1\rangle$ and $|0\rangle$. These energy differences are established by an external magnetic field, which also sets the frequency of the target rf-field that can be sensed. This is, when using the $|\acute{0}\rangle \leftrightarrow |1\rangle$ transition we can sense external fields of a frequency $\omega_1 - \omega_0 \approx \frac{\gamma_e B_z}{2} - \frac{\gamma_e^2}{4A} B_z^2$ while, if we use the $|\acute{0}\rangle \leftrightarrow |-1\rangle$ spin transition, the $^{171}\text{Yb}^+$ sensor captures rf-radiation at a frequency $\omega_0 - \omega_{-1} \approx \frac{\gamma_e B_z}{2} + \frac{\gamma_e^2}{4A} B_z^2$, see Eqs. (S15).

Both frequency differences depend on the B_z field magnitude. For example, in Ref. [S6], B_z is of the order of ≈ 1 mT allowing to measure rf signals around 14 MHz. Sensing signals with lower frequencies would require a reduction of the external magnetic field B_z since $\omega_1 - \omega_0$ and $\omega_0 - \omega_{-1}$ are proportional to B_z . However, low values for B_z leads to a weaker application of the RWA to the oscillating terms in Eq. (S25), thus to a failure of the whole sensing scheme.

A more realistic approach should consider the following Hamiltonian

$$\begin{aligned}
H = & \omega_1|1\rangle\langle 1| + \omega_0|\acute{0}\rangle\langle\acute{0}| + \omega_{-1}|-1\rangle\langle -1| + \omega_0|0\rangle\langle 0| + \mu(t)(|1\rangle\langle 1| - |-1\rangle\langle -1|) \\
& + \Omega \left[|1\rangle\langle\acute{0}| - |1\rangle\langle 0| + |\acute{0}\rangle\langle -1| + |0\rangle\langle -1| + \text{H.c.} \right] \cos(\omega_1^{\text{mw}}t + \phi_1) \\
& + \Omega \left[|1\rangle\langle\acute{0}| - |1\rangle\langle 0| + |\acute{0}\rangle\langle -1| + |0\rangle\langle -1| + \text{H.c.} \right] \cos(\omega_2^{\text{mw}}t + \phi_2) \\
& + \Omega_{\text{tg}} \left[|1\rangle\langle\acute{0}| - |1\rangle\langle 0| + |\acute{0}\rangle\langle -1| + |0\rangle\langle -1| + \text{H.c.} \right] \cos(\omega_{\text{tg}}t). \tag{S29}
\end{aligned}$$

We proceed as in the previous subsection, that is, we move to a rotating frame w.r.t. the free-energy-terms $H_0 = \omega_1|1\rangle\langle 1| + \omega_0|\acute{0}\rangle\langle\acute{0}| + \omega_{-1}|-1\rangle\langle -1| + \omega_0|0\rangle\langle 0|$. Furthermore, we select the MW control parameters such that $\omega_1^{\text{mw}} = \omega_1 - \omega_0$, $\omega_2^{\text{mw}} = \omega_{-1} - \omega_0$, $\phi_1 = \pi$ and $\phi_2 = 0$. Then, if we neglect counter rotating terms oscillating at a GHz rate we have

$$\begin{aligned}
H = & \mu(t)(|1\rangle\langle 1| - |-1\rangle\langle -1|) + \frac{\Omega}{2} \left[|1\rangle\langle 0| + |-1\rangle\langle 0| + \text{H.c.} \right] - \frac{\Omega}{2} \left[|1\rangle\langle 0| e^{i\gamma_e B_z t} + |-1\rangle\langle 0| e^{-i\gamma_e B_z t} + \text{H.c.} \right] \\
& + \Omega_{\text{tg}} \left[|1\rangle\langle\acute{0}| e^{i(\omega_1 - \omega_0)t} - |1\rangle\langle 0| e^{i(\omega_1 - \omega_0)t} + |\acute{0}\rangle\langle -1| e^{i(\omega_0 - \omega_{-1})t} + |0\rangle\langle -1| e^{i(\omega_0 - \omega_{-1})t} + \text{H.c.} \right] \cos(\omega_{\text{tg}}t). \tag{S30}
\end{aligned}$$

In the qubit basis (S23) the first line of the above Hamiltonian transforms to

$$\begin{aligned}
& \frac{-\mu(t)}{\sqrt{2}} (|D\rangle\langle u| + |D\rangle\langle d| + \text{H.c.}) + \frac{\Omega}{\sqrt{2}} (|u\rangle\langle u| - |d\rangle\langle d|) \\
& - \left[\frac{\Omega}{2\sqrt{2}} (|u\rangle\langle u| - |d\rangle\langle d|) + \frac{\Omega}{4} (|u\rangle\langle D| + |D\rangle\langle d|) - \frac{\Omega}{4} (|D\rangle\langle u| + |d\rangle\langle D|) \right] e^{i\gamma_e B_z t} + \text{H.c.} \tag{S31}
\end{aligned}$$

Now, if we want to use the $|\acute{0}\rangle \leftrightarrow |1\rangle$ spin transition as the detecting one and by taking into account that there could be energy deviations ξ in the frequency of the target signal of the kind $\omega_{\text{tg}} = \omega_1 - \omega_0 + \xi$, the second line of Hamiltonian (S30) is

$$\begin{aligned}
& \frac{\Omega_{\text{tg}}}{2} (|1\rangle\langle\acute{0}| e^{-i\xi t} + |\acute{0}\rangle\langle 1| e^{i\xi t}) \\
& + \frac{\Omega_{\text{tg}}}{2} (|1\rangle\langle\acute{0}| e^{2i(\omega_1 - \omega_0)t} e^{i\xi t} + \text{H.c.}) \\
& + \frac{\Omega_{\text{tg}}}{2} (|\acute{0}\rangle\langle -1| e^{i(\omega_1 - \omega_{-1})t} e^{i\xi t} + \text{H.c.}) \\
& + \frac{\Omega_{\text{tg}}}{2} (|\acute{0}\rangle\langle -1| e^{i(2\omega_0 - \omega_1 - \omega_{-1})t} e^{-i\xi t} + \text{H.c.}). \tag{S32}
\end{aligned}$$

If we use the basis $\{|u\rangle, |d\rangle, |D\rangle, |\acute{0}\rangle\}$ we get that the previous expression is

$$\begin{aligned}
& \left[\frac{\Omega_{\text{tg}}}{4} (|u\rangle\langle\acute{0}| + |d\rangle\langle\acute{0}|) - \frac{\Omega_{\text{tg}}}{2\sqrt{2}} |D\rangle\langle\acute{0}| \right] e^{-i\xi t} + \text{H.c.} \\
& + \frac{\Omega_{\text{tg}}}{2} \left(\frac{1}{2} |u\rangle\langle\acute{0}| + \frac{1}{2} |d\rangle\langle\acute{0}| - \frac{1}{\sqrt{2}} |D\rangle\langle\acute{0}| \right) e^{2i(\omega_1 - \omega_0)t} e^{i\xi t} + \text{H.c.} \\
& + \frac{\Omega_{\text{tg}}}{2} \left(\frac{1}{2} |\acute{0}\rangle\langle u| + \frac{1}{2} |\acute{0}\rangle\langle d| + \frac{1}{\sqrt{2}} |\acute{0}\rangle\langle D| \right) e^{i(\omega_1 - \omega_{-1})t} e^{i\xi t} + \text{H.c.} \\
& + \frac{\Omega_{\text{tg}}}{2} \left(\frac{1}{2} |\acute{0}\rangle\langle u| + \frac{1}{2} |\acute{0}\rangle\langle d| + \frac{1}{\sqrt{2}} |\acute{0}\rangle\langle D| \right) e^{i(2\omega_0 - \omega_1 - \omega_{-1})t} e^{-i\xi t} + \text{H.c.} \tag{S33}
\end{aligned}$$

Then, the final target Hamiltonian is

$$\begin{aligned}
H = & \frac{-\mu(t)}{\sqrt{2}}(|D\rangle\langle u| + |D\rangle\langle d| + \text{H.c.}) + \frac{\Omega}{\sqrt{2}}(|u\rangle\langle u| - |d\rangle\langle d|) \\
& - \left[\frac{\Omega}{2\sqrt{2}}(|u\rangle\langle u| - |d\rangle\langle d|) + \frac{\Omega}{4}(|u\rangle\langle D| + |D\rangle\langle d|) - \frac{\Omega}{4}(|D\rangle\langle u| + |d\rangle\langle D|) \right] e^{i\gamma_e B_z t} + \text{H.c.} \\
& + \left[\frac{\Omega_{\text{tg}}}{4}(|u\rangle\langle \acute{0}| + |d\rangle\langle \acute{0}|) - \frac{\Omega_{\text{tg}}}{2\sqrt{2}}|D\rangle\langle \acute{0}| \right] e^{-i\xi t} + \text{H.c.} \\
& + \frac{\Omega_{\text{tg}}}{2} \left(\frac{1}{2}|u\rangle\langle \acute{0}| + \frac{1}{2}|d\rangle\langle \acute{0}| - \frac{1}{\sqrt{2}}|D\rangle\langle \acute{0}| \right) e^{2i(\omega_1 - \omega_0)t} e^{i\xi t} + \text{H.c.} \\
& + \frac{\Omega_{\text{tg}}}{2} \left(\frac{1}{2}|\acute{0}\rangle\langle u| + \frac{1}{2}|\acute{0}\rangle\langle d| + \frac{1}{\sqrt{2}}|\acute{0}\rangle\langle D| \right) e^{i(\omega_1 - \omega_{-1})t} e^{i\xi t} + \text{H.c.} \\
& + \frac{\Omega_{\text{tg}}}{2} \left(\frac{1}{2}|\acute{0}\rangle\langle u| + \frac{1}{2}|\acute{0}\rangle\langle d| + \frac{1}{\sqrt{2}}|\acute{0}\rangle\langle D| \right) e^{i(2\omega_0 - \omega_1 - \omega_{-1})t} e^{-i\xi t} + \text{H.c.}
\end{aligned} \tag{S34}$$

Or, if we use the relations (cf. **Section I**)

$$\begin{aligned}
\omega_1 - \omega_0 & \approx \frac{\gamma_e B_z}{2} - \frac{\gamma_e^2}{4A} B_z^2, \\
\omega_1 - \omega_0 & \approx A + \frac{\gamma_e B_z}{2} + \frac{\gamma_e^2}{4A} B_z^2, \\
\omega_0 - \omega_{-1} & \approx \frac{\gamma_e B_z}{2} + \frac{\gamma_e^2}{4A} B_z^2, \\
\omega_{-1} - \omega_0 & \approx A - \frac{\gamma_e B_z}{2} + \frac{\gamma_e^2}{4A} B_z^2,
\end{aligned} \tag{S35}$$

the above Hamiltonian reads

$$\begin{aligned}
H = & \frac{-\mu(t)}{\sqrt{2}}(|D\rangle\langle u| + |D\rangle\langle d| + \text{H.c.}) + \frac{\Omega}{\sqrt{2}}(|u\rangle\langle u| - |d\rangle\langle d|) \\
& - \left[\frac{\Omega}{2\sqrt{2}}(|u\rangle\langle u| - |d\rangle\langle d|) + \frac{\Omega}{4}(|u\rangle\langle D| + |D\rangle\langle d|) - \frac{\Omega}{4}(|D\rangle\langle u| + |d\rangle\langle D|) \right] e^{i\gamma_e B_z t} + \text{H.c.} \\
& + \left[\frac{\Omega_{\text{tg}}}{4}(|u\rangle\langle \acute{0}| + |d\rangle\langle \acute{0}|) - \frac{\Omega_{\text{tg}}}{2\sqrt{2}}|D\rangle\langle \acute{0}| \right] e^{-i\xi t} + \text{H.c.} \\
& + \frac{\Omega_{\text{tg}}}{2} \left(\frac{1}{2}|u\rangle\langle \acute{0}| + \frac{1}{2}|d\rangle\langle \acute{0}| - \frac{1}{\sqrt{2}}|D\rangle\langle \acute{0}| \right) e^{2i\left(\frac{\gamma_e B_z}{2} - \frac{\gamma_e^2}{4A} B_z^2\right)t} e^{i\xi t} + \text{H.c.} \\
& + \frac{\Omega_{\text{tg}}}{2} \left(\frac{1}{2}|\acute{0}\rangle\langle u| + \frac{1}{2}|\acute{0}\rangle\langle d| + \frac{1}{\sqrt{2}}|\acute{0}\rangle\langle D| \right) e^{i\gamma_e B_z t} e^{i\xi t} + \text{H.c.} \\
& + \frac{\Omega_{\text{tg}}}{2} \left(\frac{1}{2}|\acute{0}\rangle\langle u| + \frac{1}{2}|\acute{0}\rangle\langle d| + \frac{1}{\sqrt{2}}|\acute{0}\rangle\langle D| \right) e^{i\frac{\gamma_e^2}{2A} B_z^2 t} e^{-i\xi t} + \text{H.c.},
\end{aligned} \tag{S36}$$

which is denoted as H_r and given in Eq. (A1) of the main text.

III. DEVIATION FROM RABI OSCILLATIONS

From Eq. (S36), one can already notice that the sensor will soon depart from displaying the ideal coherent Rabi oscillations predicted by Eq. (S28) when the rf-signal has either a low frequency such that the RWA cannot be safely applied, a possible detuning w.r.t. the resonant condition $\omega_{\text{tg}} = \omega_1 - \omega_0 + \xi$ with $|\xi| \ll \omega_{\text{tg}}$ s.t. $|\xi| > 0$, and/or a large Rabi frequency, $\Omega_{\text{tg}} \sim \Omega$.

In particular, as discussed in [S6], fields with a frequency of $\omega_{\text{tg}} = 2\pi \times 14$ MHz can be measured with high precision, whose amplitude can be up to few kHz, i.e. $\Omega_{\text{tg}} \lesssim 2\pi \times 3.3$ kHz. Note that the Rabi frequencies for the microwave driving the transitions $|0\rangle \leftrightarrow |1\rangle$ and $|0\rangle \leftrightarrow |-1\rangle$ amount to $\Omega = 2\pi \times 37.27$ kHz, which grants a robust decoupling w.r.t. magnetic field fluctuations. In Fig. S2 we show the evolution of $P_D(t)$ for different parameters s.t. $P_D(0) = 1$, keeping $\xi = 0$ and starting with $\Omega_{\text{tg}} = 2\pi \times 1$ kHz and $B_z = 10$ G ($\omega_{\text{tg}} \approx 2\pi \times 14$ MHz) in which $P_D(t)$ can be well approximated by $P_D(t) \approx \cos^2(\Omega_{\text{tg}} t / \sqrt{8})$, as used in [S6] which follows from Eq. (S28), and as function of time rescaled by $t_R = 2\sqrt{2}\pi/\Omega_{\text{tg}}$ (the time of a full Rabi oscillation within the

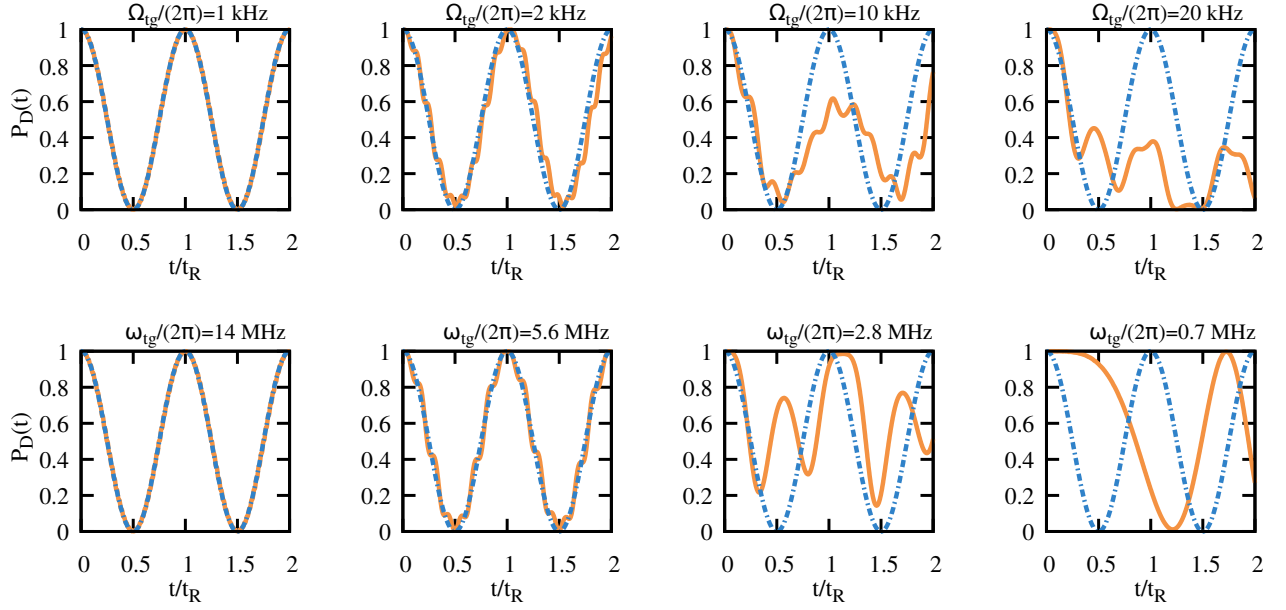


FIG. S2. Dynamics of $P_D(t)$ with $P_D(0) = 1$ using the full Hamiltonian H_r , Eq. (S36) (solid orange line) and its approximated expression, $P_D(t) \approx \cos^2(\Omega_{tg}t/\sqrt{8})$ (dashed blue line), for different parameter regimes and $\xi = 0$. The left panels, top and bottom, correspond to $\omega_{tg} \approx 2\pi \times 14$ MHz with $\Omega_{tg} = 2\pi \times 1$ kHz, a case within the validity discussed in [S6]. Top row shows the effect of increasing Ω_{tg} (from left to right), i.e., 2, 10 and 20 kHz (keeping fixed $\omega_{tg} \approx 2\pi \times 14$ MHz). The bottom row shows the effect of reducing B_z (i.e., reducing ω_{tg} and keeping fixed $\Omega_{tg} = 2\pi \times 1$ kHz), from left to right: 5.6, 2.8 and 0.7 MHz.

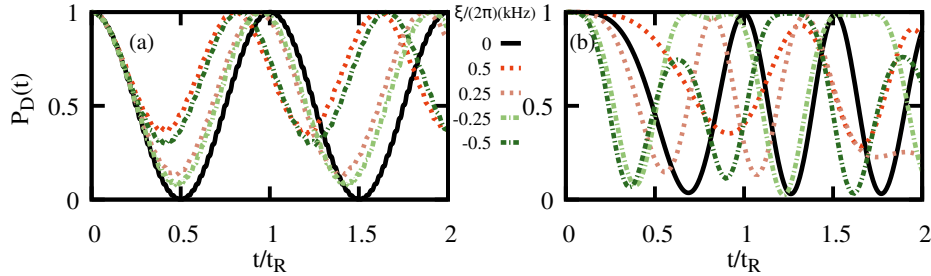


FIG. S3. Dynamics of $P_D(t)$ with $P_D(0) = 1$ using the full Hamiltonian H_r , Eq. (S36), for (a) $\Omega_{tg} = 2\pi \times 1$ kHz and $\omega_{tg} \approx 2\pi \times 14$ MHz and (b) $\Omega_{tg} = 2\pi \times 2$ kHz and $\omega_{tg} \approx 2\pi \times 2.8$ MHz, for different detunings $\xi/(2\pi) = 0$ (solid black), 0.5 kHz (dotted red), 0.25 kHz (dotted light red), -0.25 kHz (dashed light green) and -0.5 kHz (dashed dark green).

approximated dynamics). Then, either increasing Ω_{tg} (top panels) or decreasing B_z (i.e. ω_{tg}) (bottom panels) leads to a departure from the RWA and more structured dynamics are observed. See caption for the considered parameters.

The impact of a detuned signal with respect to the resonant frequency splitting $\omega_1 - \omega_0$ by an amount ξ is illustrated in Fig. S3. We show two cases, namely, when the RWAs can be safely applied ($\Omega_{tg} = 2\pi \times 1$ kHz and $\omega_{tg} \approx 2\pi \times 14$ MHz) (cf. Fig. S2) and for a case in which the dynamics is more structured ($\Omega_{tg} = 2\pi \times 2$ kHz and $\omega_{tg} \approx 2\pi \times 2.8$ MHz). For larger detunings, the rf-signal is not capable of producing transitions in the sensor, and thus the population remains constant $P_D(t) \approx 1$.

IV. MAGNETIC-FIELD AND AMPLITUDE FLUCTUATIONS

The quantum sensor is prone to magnetic-field as well as intensity fluctuations of the Rabi frequencies. The magnetic-field fluctuations enter in the Hamiltonian as $\mu(t)(|1\rangle\langle 1| - | -1\rangle\langle -1|)$, that transforms in the final Hamiltonian to terms producing spurious transitions in the subspace spanned by $\{|u\rangle, |d\rangle, |D\rangle\}$ (cf. Eq. (A1) in the main text or Eq. (S36) here). Such fluctuations

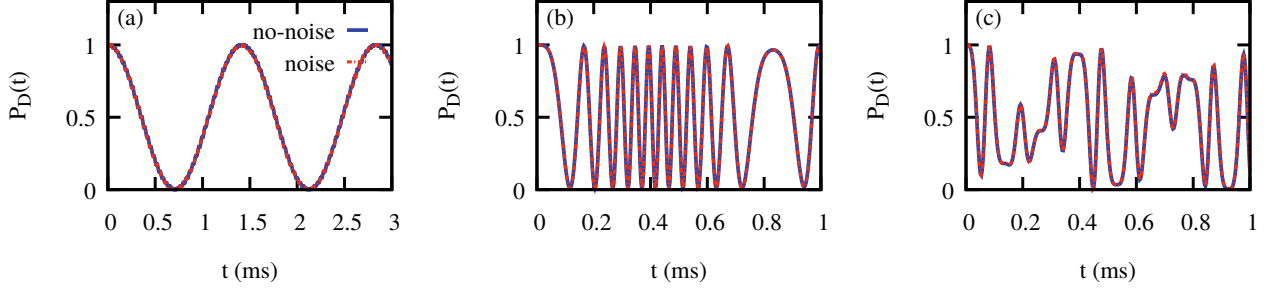


FIG. S4. Dynamics of $P_D(t)$ with $P_D(0) = 1$ using the full Hamiltonian H_r , Eq. (S36) with (dashed red line) and without (solid blue line) noises (magnetic-field and intensity fluctuations), as commented in **Section IV**. The results are equivalent, i.e., these noise sources do produce a significant impact in this time scale. The noisy dynamics has been obtained averaging 100 stochastic repetitions. Panel (a) corresponds to the case I in main text, for $\Omega_g = 2\pi \times 1$ kHz, $\omega_g = 2\pi \times 14$ MHz and $\xi = 0$, while (b) and (c) clearly deviate from the coherent Rabi oscillations, with $\Omega_g = 2\pi \times 15$ kHz, $\omega_g = 2\pi \times 2.8$ MHz and $\xi = 0$, and $\Omega_g = 2\pi \times 12$ kHz, $\omega_g = 2\pi \times 7$ MHz and $\xi = 2\pi \times 0.1$ kHz (cf. Fig. 3 in the main text), respectively.

can be well described by a stochastic Orstein-Uhlenbeck process $\mu(t)$ [S7–S9]. This Gaussian noise is fully characterized by its correlation time τ_μ and intensity σ_μ , with $\langle \mu(t) \rangle = 0$ and $\langle \mu(t + \delta t)\mu(t) \rangle = \sigma_\mu^2 e^{-\delta t/\tau_\mu}$ for $\delta t \geq 0$, and it allows for an exact update formula [S8, S9],

$$\mu(t + \delta t) = \mu(t)e^{-\delta t/\tau_\mu} + \sigma_\mu \left(1 - e^{-2\delta t/\tau_\mu}\right)^{1/2} N(t), \quad (\text{S37})$$

with $N(t)$ denoting a random variable drawn from a normal distribution, $\langle N(t) \rangle = 0$ and $\langle N(t)N(t + t') \rangle = \delta(t - t')$. This noise fulfills the properties of a continuous Markov process. From the previous update formula, one can calculate

$$\langle \zeta^2(t) \rangle = \sigma_\mu^2 \tau_\mu^2 \left[\frac{2t}{\tau_m} - 3 + 4e^{-t/\tau_m} - e^{-2t/\tau_m} \right] \quad (\text{S38})$$

with $\zeta(t) = \int_0^t ds \mu(s)$. In this manner, it is easy to see that a state prepared in a $|1\rangle \pm |-1\rangle$ superposition evolving under $\mu(t)(|1\rangle\langle 1| - |-1\rangle\langle -1|)$ will decay as $\langle \sigma_{x;1,-1}(t) \rangle = e^{-\frac{1}{2}\langle \zeta^2(t) \rangle}$, where $\sigma_{x;1,-1} = |1\rangle\langle -1| + \text{H.c.}$. The decoherence time induced by these magnetic-field fluctuations is defined as $\langle \sigma_{x;1,-1}(T_2) \rangle = e^{-1}$, so that

$$\sigma_\mu = \left(\tau_\mu(T_2 - \tau_\mu(3/2 - 2e^{-T_2/\tau_\mu} + 1/2e^{-2T_2/\tau_\mu})) \right)^{-1}. \quad (\text{S39})$$

For an exponential decay of the coherence, as typically observed in experiments, $\langle \sigma_{x;1,-1}(t) \rangle \propto e^{-t/T_2}$, one obtains the condition $\tau_m \ll T_2$, which in turn leads to $\sigma \approx 1/(T_2\tau_m)$. Here we have used $T_2 = 5.3$ ms as measured in [S6], and $\tau_\mu = T_2/100$. For the intensity field fluctuations we include $\Omega \rightarrow \Omega(1 + \epsilon(t))$ where $\epsilon(t)$ again follows an Orstein-Uhlenbeck process with $\tau_\epsilon = 1$ ms and relative intensity of 2.5×10^{-3} , as given in [S10]. These two sources of noise do not produce a significant impact in the dynamics of the populations in the time scale considered here (see Ref. [S6] for experimental results). See Fig. S4 for examples showing the dynamics of the population $P_D(t)$ with and without including these noise sources.

V. SIMULATION OF AN EXPERIMENTAL ACQUISITION

Let us denote the population we are interested in measuring at time t_k by P_k . When the quantum sensor is interrogated after an evolution time t_k , one retrieves 1 with probability P_k (when found in $|D\rangle$), as considered in the main text, and 0 with probability $1 - P_k$. This binomial process allows us to obtain an estimate of P_k after repeating the measurement N_m times, which we denote here by P_k^s and reads as

$$P_k^s = \frac{1}{N_m} X_k = \frac{1}{N_m} \sum_{n=1}^{N_m} x_{n;k}, \quad (\text{S40})$$

where $x_{n;k}$ is the n th outcome, i.e., a random variable drawn from a Binomial distribution $B(1, P_k)$ with success probability P_k , such that $x_{n;k} = \{0, 1\}$ and $X_k = \sum_{n=1}^{N_m} x_{n;k}$ the number of 1's recorded at the interrogation time t_k . Only for illustration purposes,

we assign a shot-noise uncertainty to each P_k^s , which is given by $\sigma_k = \max(1/N_m, \sigma_{N_m;k}/\sqrt{N_m})$, with $\sigma_{n;k}$ the standard deviation of the list of outcomes $\{x_{1;k}, x_{2;k}, \dots, x_{N_m;k}\}$. In the limit of many outcomes, $N_m \gg 1$, it will read as $\sigma_{N_m;k} = \sqrt{P_k(1-P_k)}$ so that $\sigma_{N_m;k}/\sqrt{N_m}$ is the standard error of mean and $\sigma_k = \sigma_{N_m;k}/\sqrt{N_m}$. Note that the uncertainty $1/N_m$ gives account of the variation in the estimate P_k^s if one value is flipped, $x_{n;k} \rightarrow 1 - x_{n;k}$. More precisely, this uncertainty stems from the confidence interval in determining P_k^s that after N_m trials any has not been successful. With a 68.2% confidence interval (equivalent to 1σ in a normal distribution) the probability of P_k being 0 reads as $p(P_k^s = 0) \leq 0.318$, which for P_k close to 0, it follows that $0 \leq P_k \leq -\log(0.318)/N_m$, which can be approximated to $0 \leq P_k \leq 1/N_m$. In a similar manner, if all of the N_m trials have been successful, the same argument applies.

For reproducibility, we provide in the following the string of outcomes obtained randomly and used for the analysis shown in the main text, for both cases. For *Case I*, with $t_k = 2.83(k-1)/(N_p-1)$ ms for $k = 1, \dots, N_p$ and $N_p = 18$, we use $X_k = \{1, 1, 0, 0, 0, 1, 1, 0, 1, 0, 0, 0, 0, 0, 1, 1, 1\}$ for $N_m = 1$, $X_k = \{4, 3, 1, 1, 0, 0, 0, 2, 4, 3, 4, 2, 0, 0, 1, 2, 2, 4\}$ for $N_m = 4$, and $X_k = \{20, 18, 11, 4, 0, 2, 11, 12, 18, 20, 12, 7, 0, 0, 7, 9, 18, 20\}$ for $N_m = 20$. For *Case II*, with $t_k = 0.236(k-1)/(N_p-1)$ ms with $N_p = 20$, we use $X_k = \{4, 4, 2, 2, 1, 0, 4, 3, 2, 1, 0, 1, 0, 1, 3, 2, 1, 0, 2, 1\}$ for $N_m = 4$, $X_k = \{20, 20, 16, 11, 0, 6, 16, 20, 11, 5, 6, 2, 2, 3, 2, 9, 12, 7, 4, 7\}$ for $N_m = 20$, and $X_k = \{40, 40, 34, 22, 7, 14, 35, 38, 22, 13, 5, 5, 6, 8, 10, 22, 22, 12, 8, 11\}$ for $N_m = 40$. As commented in the main text, and presented below, we also consider a single-shot acquisition for this case, i.e. $X_k = \{1, 1, 1, 1, 0, 1, 1, 1, 1, 0, 0, 0, 0, 0, 0, 1, 0, 1, 1, 0\}$ for $N_m = 1$.

VI. BAYESIAN INFERENCE

Here we provide more examples and details of the numerical calculations presented in the main text where Bayes' rule is used to provide reliable estimators of unknown parameters based on the observed/measured data [S11, S12].

From Bayes' theorem we know that the posterior probability $p(\Theta|\mathbf{D})$ is proportional to $p(\mathbf{D}|\Theta)p(\Theta)$ (up to a normalization factor). This probability distribution contains the information we can extract from the observed data \mathbf{D} given the prior knowledge over the parameters $p(\Theta)$, and the likelihood $p(\mathbf{D}|\Theta)$. As commented in the main text, the Binomial statistics of X_k leads to

$$p(\mathbf{D}|\Theta) = \prod_{k=1}^{N_p} f(X_k, N_m, \tilde{P}_k(t_k; \Theta)) \quad \text{with} \quad f(x, n, p) = \frac{n!}{x!(n-x)!} p^x (1-p)^{(n-x)}, \quad (\text{S41})$$

where $f(x, n, p)$ denotes the probability of having observed x success outcomes from n trials from a Binomial distribution with success probability p , while $\tilde{P}_k(t_k; \Theta)$ stands for the expected population at time t_k when using Θ as the parameters in the model. The values X_k from N_m measurements at each time t_k form the observations, i.e., the data \mathbf{D} . In the following we provide more details about the first case of study presented in the main text, namely, *case I*, while more information on Markov Chain Monte Carlo methods, relevant for the *case II*, is presented in **Section VII**.

VI A. Case I

The application of the RWAs allows us to obtain an analytical expression $P_D(t) = \cos^2(\Omega_{\text{tg}}t/\sqrt{8})$ when the initial state is $|D\rangle$, i.e. $P_D(0) = 1$ [S6]. In this manner, one can easily compute Eq. (S41) and so the posterior by scanning different values of Ω_{tg} . Note that in this case, $\Theta = \{\Omega_{\text{tg}}\}$ and $\tilde{P}_k(t_k; \Theta) \rightarrow \cos^2(\Omega_{\text{tg}}t_k/(2\sqrt{2}))$. This is plotted in Fig. S5(a) for four different sets of observations \mathbf{D} containing $N_p = 21$ points, each of them obtained averaging $N_m = 5$ measurements, and generated from $\omega_{\text{tg}} = 2\pi \times 14$ MHz, $\xi = 0$ and $\Omega_{\text{tg}}^{\text{id}} = 2\pi \times 2$ kHz. The time separation between consecutive points is $t_{k+1} - t_k \approx 0.1$ ms, so that we consider Ω_{tg} up to 10 kHz (see below for a discussion). Note that reliable estimates can be obtained even in the situation of reduced number of measurements and few recorded times (cf. Fig. S5(b) and (c)).

It is well known that an equally-spaced sampling of a periodic signal can produce aliasing effects. In particular, if the time difference between two measured points is Δt , then the maximum frequency than can be inferred without aliasing is half of the sampling rate, set by the Nyquist frequency $f_f = 1/(2\Delta t)$. For a periodic signal $y(t) \propto \cos(\omega t)$, this leads to $\omega^{\text{max}} = 2\pi/(2\Delta t)$. In our case, from Eq. (3) of the main text, one finds $\Omega_{\text{tg}}^{\text{max}} = 2\pi/(\sqrt{2}\Delta t)$. For the *case I* shown in the main text, $\Delta t \approx 1/6$ ms, so that $\Omega_{\text{tg}}^{\text{max}} \approx 2\pi \times 6/\sqrt{2}$ kHz $\approx 2\pi \times 4.2$ kHz. This pre-knowledge can be included in the prior such that frequencies $\Omega_{\text{tg}} > \Omega_{\text{tg}}^{\text{max}}$ are not considered, i.e. $p(\Omega_{\text{tg}} > \Omega_{\text{tg}}^{\text{max}}) = 0$. See Fig. S6 for an illustration of this effect. The noisy signal has been obtained simulating an experiment with $N_p = 21$ equally-spaced points, $N_m = 10$ measurement repetitions per point and $\Omega_{\text{tg}} = 2\pi \times 7$ Hz, fixing $\xi = 0$ and $\omega_{\text{tg}} = 2\pi \times 14$ MHz, from $t = 0$ to $t_f = 500$ ms, similar to one case explored in [S6]. For an initial state $|D\rangle$, it follows $P_D(t) \approx \cos^2(\Omega_{\text{tg}}t/\sqrt{8})$. Scanning the range $\Omega_{\text{tg}} \in 2\pi[0.1, 100]$ Hz, one finds that the posterior $p(\Omega_{\text{tg}}|\mathbf{D})$ features three peaks at the values $2\pi \times 7$, $2\pi \times 50$ and $2\pi \times 63$ Hz. Taking into account these overfitted solutions, one finds $\Omega_{\text{tg}}^{\text{est}} \approx 2\pi \times 40(24)$ Hz. A simple post analysis however allows us to discard such overfitted solutions or frequencies above $\Omega_{\text{tg}}^{\text{max}}$ (cf. Fig. S6(b))

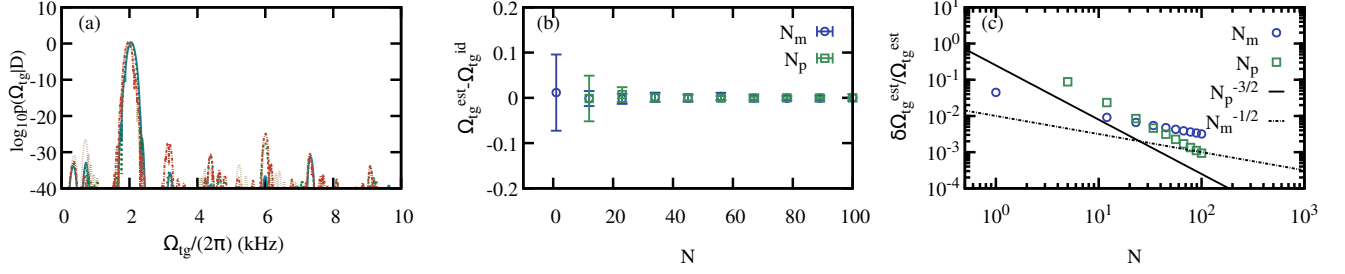


FIG. S5. (a) Logarithm of the posterior probability distribution over the amplitude Ω_{tg} , $\log_{10} p(\Omega_{\text{tg}}|\mathbf{D})$ given four different and independent observations \mathbf{D} , with $N_p = 21$, $N_m = 5$ and generated from $\omega_{\text{tg}} = 2\pi \times 14$ MHz, $\xi = 0$ and $\Omega_{\text{tg}}^{\text{id}} = 2\pi \times 2$ kHz. (b) Difference between $\Omega_{\text{tg}}^{\text{est}}$, obtained upon an average of 40 runs (i.e. over 40 independent sets of observations \mathbf{D}), and $\Omega_{\text{tg}}^{\text{id}}$ (in kHz), as function of $N = \{N_m, N_p\}$, namely, increasing the number of measurements N_m per point and keeping $N_p = 21$ points and $t_f = 3/\sqrt{2}$ ms (blue circles), and increasing the number of points N_p (and thus $t'_f = t_f N_p/21$ so that $t_{k+1} - t_k \approx 0.1$ ms) keeping $N_m = 10$ measurements per point (green squares). In panel (c) we show the precision of the estimated Rabi frequency $\delta\Omega_{\text{tg}}^{\text{est}}/\Omega_{\text{tg}}^{\text{est}}$ as $N = \{N_m, N_p\}$ increases. The lines are guides to the eyes marking different scaling with N .

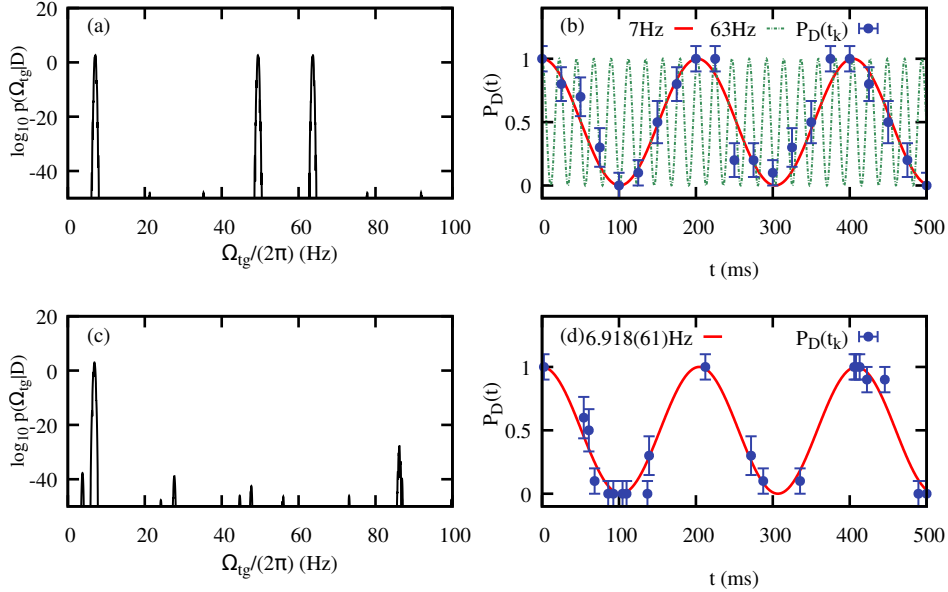


FIG. S6. (a) Logarithm of the posterior probability distribution over the amplitude Ω_{tg} , $\log_{10} p(\Omega_{\text{tg}}|\mathbf{D})$ given the data \mathbf{D} in the panel (b), assuming an uninformative prior in $\Omega_{\text{tg}} \in 2\pi[0.1, 100]$ Hz. Note that the data has been obtained with $\Omega_{\text{tg}} = 2\pi \times 7$ Hz, so that the peaks appearing at $2\pi \times 50$ and $2\pi \times 63$ Hz are spurious. In (b) we show the equally-space observed data (points) and the ideal signal $\Omega_{\text{tg}} = 2\pi \times 7$ Hz, and one of the resulting overfitted predictions, e.g. $2\pi \times 63$ Hz. Same plots in (c) and (d) but using a random time sampling in $t \in [0, t_f]$. In (d) the observed data \mathbf{D} , i.e. $P_k^s(t_k)$ with uncertainty σ_k , is plotted together with the predicted one $P_D(t) = \cos^2(\Omega_{\text{tg}}^{\text{est}} t / \sqrt{8})$ (red). See text for further details.

by discarding values $\Omega_{\text{tg}} > 2\pi/(\sqrt{2}\Delta t)$, so that one obtains $\Omega_{\text{tg}}^{\text{est}} \approx 2\pi \times 7.147(42)$ Hz. We comment that the impact of such aliasing effects can be reduced through non-equal time sampling, such as randomly selecting the instances t_k at which the sensor is interrogated. See Fig. S6 for the same parameters as before but where the sampling times t_k have been selected randomly in the interval $[0, t_f]$. In this manner, with the data shown in Fig. S6(d), one finds $\Omega_{\text{tg}}^{\text{est}} = 2\pi \times 6.918(61)$ Hz when inspecting in $\Omega_{\text{tg}} \in 2\pi[0.1, 100]$ Hz.

It is worth mentioning that standard least-squares regression techniques can be applied here to fit the observations or data \mathbf{D} to $P_D(t) = \cos^2(\Omega_{\text{tg}} t / \sqrt{8})$. Note however that the uncertainties σ_k will be in general different for each the N_p points. Moreover, any pre-knowledge or bias about Ω_{tg} , i.e. any informative prior $p(\Theta)$, makes the least-squares fit inapplicable. In addition, as posteriors need not be Gaussian, the Bayesian-inference based method allows us to gain more information of the unknown parameter.

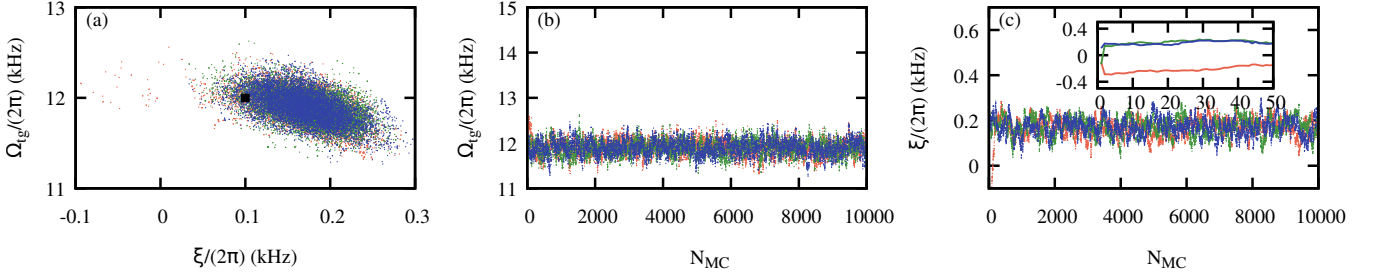


FIG. S7. (a) Scatter plot of the recorded points during three independent MCMC as for the case considered in the main text (cf. Fig. (3)). Panels (b) and (c) illustrate the evolution of the chain as a function of the number of Monte Carlo steps. Inset in (c) show the burn-in regime for ξ , in which the initial points jump until reaching the convergence region with good mixing.

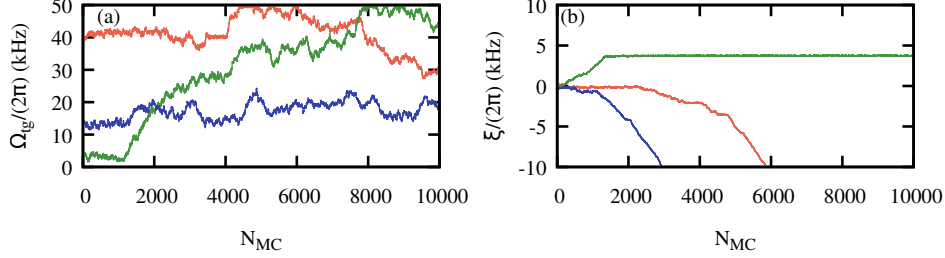


FIG. S8. Results of three independent MCMC for a single shot acquisition ($N_m = 1$) for the same parameters as used in Fig. 3(a) of the main text. The recorded MCMC steps for Ω_{ig} (a) and ξ (b). Due to the large shot noise, and the non-harmonic sensor response, the chains do not converge.

VII. MARKOV CHAIN MONTE CARLO

As explained in the main text, when the determination of the posterior probability distributions of the unknown parameters becomes complex and numerically demanding, one may resort to Markov Chain Monte Carlo (MCMC) methods [S11, S13] for an efficient sampling of such distributions. Here we perform the sampling using a Metropolis algorithm, as explained in the main text. Fig. S7 shows an additional Markov chain for the same case considered in the Fig. (3) of the main text. The trace plots in Figs. S7(b) and (c) show the evolution of the three independent Markov chains, which achieve a good convergence and mixing upon 100 Monte Carlo steps. In order to speed up the convergence of the Markov chain, we perform 100 Metropolis pre-steps using the prior probability distributions to propose the subsequent step. The results shown in the main text have been obtained removing the first 200 steps of the MCMC after the 100 of the (burn-in). The effective size of the Markov chain is approximately $N_{\text{MC}}/2$. Recall that the prior probability distribution $p(\Omega_{\text{ig}})$ is flat, i.e., uninformative in the region of interest, $0 \leq \Omega_{\text{ig}} \leq 2\pi \times 50$ kHz, while we take $p(\xi) = \mathcal{N}(0, \sigma_\xi^2)$ with $\sigma_\xi = 2\pi \times 0.1$ kHz. The maximum value for the Rabi frequency is again related to the Nyquist frequency (see above) as $1/\Delta t \approx 80$ kHz for the *case II*, so that $\Omega_{\text{ig}}^{\text{max}} \approx 2\pi \times 57$ kHz. The steps during the MCMC are performed using σ_Ω^2 and σ_ξ^2 , where $\sigma_\Omega = 2\pi \times 1$ kHz is found to give a good effective size. For slow converging cases one may rely to adaptive sampling, reducing both σ_Ω and σ_ξ , or by employing a different algorithm (e.g. Metropolis-Hastings) [S13].

Finally, we show in Fig. S8 the results of three independent MCMC when $N_m = 1$ and same parameters as in Fig. 3 of the main text. Due to the large shot noise and the non-harmonic response of the quantum sensor, there is no convergence in the MCMC. Almost any pair of values $\Theta = \{\Omega_{\text{ig}}, \xi\}$ provides a signal $\hat{P}_k(t_k; \Theta)$ from which the observations \mathbf{D} could have been obtained.

VIII. FAST FOURIER TRANSFORM ANALYSIS AND LEAST-SQUARES FITS

The Fast Fourier Transform (FFT) allows for the determination of the relevant frequencies of a signal. Here we show the results of the FFT for the two cases studied in the main text, namely, performing the FFT of the data \mathbf{D} shown in Fig. 2(a) (case I) and Fig. 3(a) (case II). In particular, since the populations in \mathbf{D} oscillate between 0 and 1, we shift and normalize the data to be within -1 and 1 to suppress the zero frequency component. In Fig. S9 we show the spectrum of \mathbf{D} on Fourier components

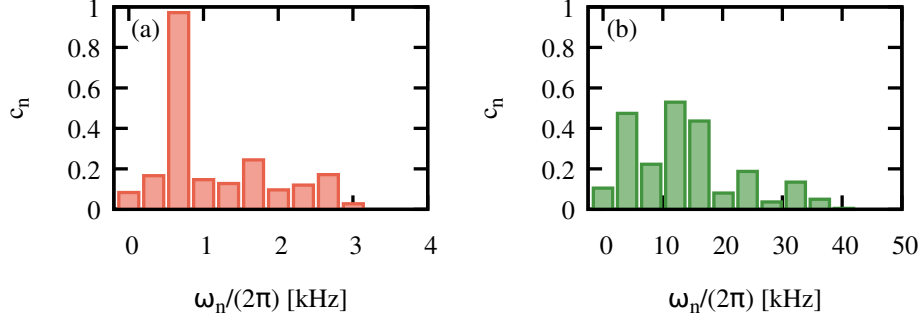


FIG. S9. FFT spectrum of the data shown in Fig. 2(a) and Fig. 3(b) of the main text, plotted in (a) and (b), respectively. In (a), for the case I, we identify a relevant frequency for which $c_n \approx 1$, whose value is $\omega_n = 2\pi \times 0.6678$ kHz. In (b), which corresponds to the case II studied in the main text, the FFT provides different relevant frequencies, which together with the lack of a simple relation between $P_D(t)$ and Ω_{tg} challenges the identification of Ω_{tg} , as well as of potential detunings ξ .

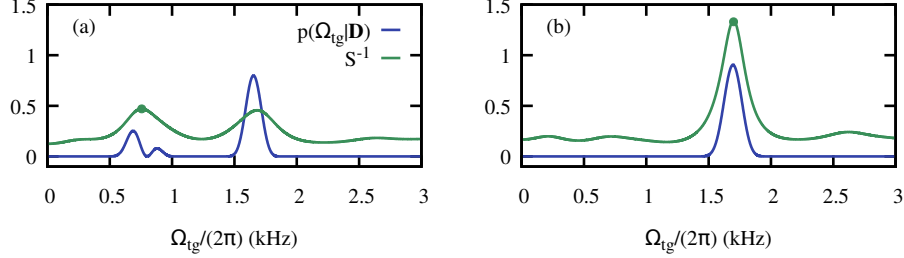


FIG. S10. Comparison between S^{-1} for the least-squares fit (green) and the posterior distribution $p(\Omega_{\text{tg}}|\mathbf{D})$ (blue) using a Bayesian analysis for two different realizations (a) and (b) with $\Omega_{\text{tg}} = 2\pi \times 1.6$ kHz and $N_m = 1$ (single shot measurements) and $N_p = 15$. The least squares maximizes S^{-1} . In both cases, the solid point indicates the estimator using least-squares $\Omega_{\text{tg}}^{\text{est:LQ}}$. In (a), the data \mathbf{D} is such that S^{-1} exhibits a maximum at $\Omega_{\text{tg}}^{\text{est}} \approx 2\pi \times 0.76$ kHz while the posterior still reveals a dominant contribution close to the true value $\Omega_{\text{tg}} = 2\pi \times 1.6$ kHz. In (b) we show a particular case in which the least-squares fit to the data \mathbf{D} provides a more accurate estimator, $\Omega_{\text{tg}}^{\text{est:LQ}} = 2\pi \times 1.699(57)$ kHz, than its Bayesian counterpart, $\Omega_{\text{tg}}^{\text{est:Bayes}} = 2\pi \times 1.695(69)$ kHz. In average, however, we find $\delta\Omega_{\text{tg}}^{\text{est:Bayes}}/\delta\Omega_{\text{tg}}^{\text{est:LQ}} \approx 0.8$. The data is $X_k = \{1, 1, 1, 0, 0, 0, 0, 1, 0, 0, 0, 0, 1, 1, 1\}$ and $X_k = \{1, 1, 0, 0, 0, 1, 1, 1, 1, 0, 0, 0, 1, 1, 1\}$, and for (a) and (b), respectively, and for the times $t_k = 1.76(k-1)/(N_p-1)$ ms.

c_n at frequency ω_n .

For the case I we find that $P_D(t)$ and Ω_{tg} are related through Eq. (3) of the main text. Hence, one can obtain an estimate of Ω_{tg} based on the FFT. In particular, here we see that the FFT of the data \mathbf{D} leads to a predominant frequency with a weight close to one, thus revealing a monochromatic signal (cf. Fig. S9(a)). The maximum corresponds to $\omega_{\text{max}} = 2\pi \times 0.6678$ kHz. From $P_D(t) = \cos^2(\pi t/(2\pi\sqrt{2}/\Omega_{\text{tg}}))$, it is easy to find $\Omega_{\text{tg}}^{\text{est}} = \sqrt{2}\omega_{\text{max}}$. A rough uncertainty of this estimator is taken as $\delta\omega/4$ where $\delta\omega$ is the frequency resolution of the FFT, so that $\Omega_{\text{tg}}^{\text{est}} = 2\pi \times 0.94(12)$ kHz. This estimated value, although compatible with the ideal one, $\Omega_{\text{tg}} = 2\pi \times 1$ kHz, is less accurate than the one obtained via Bayesian inference. In this case, a least-squares fit of the data \mathbf{D} to the expression $P_D(t) = \cos^2(\Omega_{\text{tg}}t/\sqrt{8})$ allows us to find estimates for Ω_{tg} . In particular, for $N_m = 4$ measurements per point (see above for the actual string of outcomes) we obtain $\Omega_{\text{tg}} = 2\pi \times 0.947(20)$. The uncertainty corresponds to a confidence interval of 68%, i.e. to 1σ .

We find that least-squares fits yield, in average, a less accurate estimator $\Omega_{\text{tg}}^{\text{est}}$ than its Bayesian counterpart. For that we simulate 100 realizations where we arbitrarily chose $\Omega_{\text{tg}} = 2\pi \times 1.6$ kHz. For $N_m = 1$ (single shot measurements) and $N_p = 15$ we find that, in average, $\delta\Omega_{\text{tg}}^{\text{est:Bayes}}/\delta\Omega_{\text{tg}}^{\text{est:LQ}} \approx 0.8$ in the region $\Omega_{\text{tg}} \in 2\pi \times \{1, 2\}$ kHz, where LQ stands for least-squares fit. Similar results are also observed, in average, for other cases considered in the main text, namely, $N_m = N_p = 15$ and $N_m = 20$ with $N_p = 15$ and for different values of Ω_{tg} . Yet, it is worth remarking that this holds in average, so it is still possible that the least-squares fit gives a more precise estimator than the Bayesian analysis for a particular realization. In order to remark this point, we plot in Fig. S10 the inverse of the sum of the residuals ϵ_i , i.e. $S^{-1} \equiv (\sum_{i=1}^{N_p} \epsilon_i^2)^{-1}$, together with the posterior

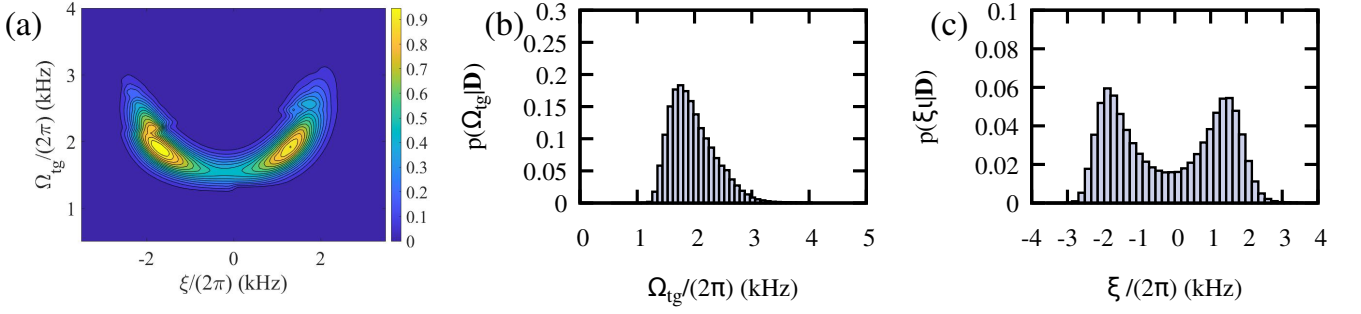


FIG. S11. (a) Posterior for the two unknown parameters ξ and Ω_{tg} when $\Omega_{\text{tg}} = 2\pi \times 2$ kHz and $\xi = -2\pi \times 1.5$ kHz with $B_z = 1$ mT, for a realization with $N_m = 4$ and $N_p = 20$. Panels (b) and (c) shown the marginals for each of these parameters, which clearly reveals a bi-modal distribution for ξ . See main text for further details. In this case we find $\Omega_{\text{tg}}^{\text{est}} = 2\pi \times 1.97(39)$ kHz.

distribution obtain for two different realizations with $N_m = 1$ and $N_p = 15$. In Fig. S10(a), the data \mathbf{D} is such that S exhibits a global minimum at $\Omega_{\text{tg}}^{\text{est:LQ}} \approx 2\pi \times 0.75$ kHz, while the posterior distribution $p(\Omega_{\text{tg}}|\mathbf{D})$ clearly reveals a peak around the true value $\Omega_{\text{tg}} = 2\pi \times 1.6$ kHz. In Fig. S10(b) we show S^{-1} and $p(\Omega_{\text{tg}}|\mathbf{D})$ for a particular realization in which the least-square fit gives a more precise estimator than through $p(\Omega_{\text{tg}}|\mathbf{D})$ (see caption for further details). Finally, we remark that the Bayesian analysis provides the posterior distribution over the parameter of interest which contains more information than just a single estimator $\Omega_{\text{tg}}^{\text{est}}$ that a FFT or least-squares fit output.

For the case II however there is no simple relation between $P_D(t)$ and Ω_{tg} and ξ . This challenges the identification of Ω_{tg} through a FFT analysis. Indeed, as shown in Fig. S9(b), the FFT spectrum reveals relevant contributions at different frequencies in a broad range of frequencies (from 5 to 20 kHz). Recall that $\Omega_{\text{tg}} = 2\pi \times 12$ kHz for this data \mathbf{D} . Moreover, this FFT analysis cannot identify potential detunings ξ w.r.t. the resonant condition. Compare this analysis with the accurate results presented in the Fig. 3 of the main text using Bayesian inference.

One may still rely on least-squares methods aiming to determine the unknown parameters, although now the data must be fitted to the numerically-computed expression $P_D(t) = \langle |D|U(t,0)|D\rangle^2$, where $U(t,0) = \mathcal{T}e^{-i\int_0^t ds H_r(s)}$ denotes the time evolution propagator of the time-dependent Hamiltonian H_r , given in Eq. (A1) of the main text. Recall that the Hamiltonian H_r depends on these unknown parameters $\{\Omega_{\text{tg}}, \xi\}$. Such non-linear fit can be performed using the subroutine `lsqcurvefit` of MATLAB. In general, the fit is not capable to modify the required starting values, as it happens when choosing $\Omega_{\text{tg}} = 2\pi \times 8$ kHz and $\xi = 2\pi \times 0.1$ kHz as initial values (rather close to the ideal frequencies 12 and 0.1 kHz, respectively). From Bayesian inference, we know that these observations are more compatible with a negative detuning, so we choose a different initial pair of values, $\Omega_{\text{tg}} = 2\pi \times 8$ kHz and $\xi = 2\pi \times -0.1$ kHz, but the fit is again incapable of finding the good solution found with our method (cf. main text), and it leads to $\Omega_{\text{tg}} = 2\pi \times 7.627$ kHz and $\xi = 2\pi \times -0.0998$ kHz, far from the Rabi frequency of 12 kHz. Moreover, even when starting close to the solution, slightly different initial values lead to different results, e.g. $\Omega_{\text{tg}} = 2\pi \times 12.73$ kHz and $\xi = 2\pi \times -0.0914$ kHz when starting from $\Omega_{\text{tg}} = 2\pi \times 15$ kHz, $\xi = 2\pi \times 0.1$, while one obtains $\Omega_{\text{tg}} = 2\pi \times 11.25$ kHz and $\xi = 2\pi \times 0.94$ kHz when starting from $\Omega_{\text{tg}} = 2\pi \times 12$ kHz and $\xi = 2\pi \times 1$. This holds for other realizations, while our Bayesian inference provides good estimates. This further demonstrates the advantage of Bayesian inference. In particular, for other 5 different realizations with $N_m = 4$ and $N_p = 20$, we obtain $\Omega_{\text{tg}}^{\text{est}} = 2\pi \times 11.79(18)$ kHz, $\xi^{\text{est}} = 2\pi \times 0.097(45)$ kHz, $\Omega_{\text{tg}}^{\text{est}} = 2\pi \times 11.95(16)$ kHz, $\xi^{\text{est}} = 2\pi \times 0.152(35)$ kHz, $\Omega_{\text{tg}}^{\text{est}} = 2\pi \times 11.48(18)$ kHz, $\xi^{\text{est}} = 2\pi \times 0.172(52)$ kHz, $\Omega_{\text{tg}}^{\text{est}} = 2\pi \times 11.87(17)$ kHz, $\xi^{\text{est}} = 2\pi \times 0.118(46)$ kHz and $\Omega_{\text{tg}}^{\text{est}} = 2\pi \times 12.09(14)$ kHz, $\xi^{\text{est}} = 2\pi \times 0.178(32)$ kHz, for each of the 5 different realizations.

Finally, and in order to emphasize the suitability of Bayesian techniques over other methods (FFT and least-squares fits) we consider a different case study, namely, $B_z = 1$ mT where the amplitude is $\Omega_{\text{tg}} = 2\pi \times 2$ kHz and a large detuning $\xi = -2\pi \times 1.5$ kHz. Again, we take $N_m = 4$ measurements for each of the $N_p = 20$ points at time $t_k = 0.25(k-1)/(N_p-1)$ ms. For this case, the prior for is a Gaussian centered at zero and $\sigma_\xi = 2\pi \times 2$ kHz. A typical posterior obtained through the Bayesian inference is shown in Fig. S11. The marginal $p(\xi|\mathbf{D})$ exhibits a bi-modal structure (cf. Fig. S11(c)), which simply cannot be tackled by standard methods (FFT or least-squares fits). Even scanning the sum of the residuals S for each pair of values Ω_{tg} and ξ , the minimum will always give a single value for each of them, regardless of the distribution. In particular, for a realization of this

case we find $\Omega_{\text{ig}}^{\text{est:LQ}} \approx 2\pi \times 1.40$ kHz, while the Bayesian inference leads to $\Omega_{\text{ig}}^{\text{est:Bayes}} = 2\pi \times 1.81(46)$ kHz.

-
- [S1] S. Olmschenk, K. C. Younge, D. L. Moehring, D. N. Matsukevich, P. Maunz, and C. Monroe, Manipulation and detection of a trapped Yb⁺ hyperfine qubit, *Phys. Rev. A* **76**, 052314 (2007).
- [S2] D. J. Griffiths, *Introduction to Quantum Mechanics* (Prentice Hall, New Jersey, 1994).
- [S3] I. Reichenbach, and I. H. Deutsch, Sideband Cooling while Preserving Coherences in the Nuclear Spin State in Group-II-like Atoms, *Phys. Rev. Lett.* **99**, 123001 (2007).
- [S4] N. Timoney, I. Baumgart, M. Johanning, A. F. Varón, M. B. Plenio, A. Retzker, and Ch. Wunderlich, Quantum gates and memory using microwave-dressed states, *Nature* **476**, 185 (2011).
- [S5] G. Mikelsons, I. Cohen, A. Retzker, and M. B. Plenio, Universal set of gates for microwave dressed-state quantum computing, *New J. Phys.* **17** 053032 (2015).
- [S6] I. Baumgart, J.-M. Cai, A. Retzker, M. B. Plenio, and Ch. Wunderlich, Ultrasensitive Magnetometer using a Single Atom, *Phys. Rev. Lett.* **116**, 240801 (2016).
- [S7] G. E. Uhlenbeck, and L. S. Ornstein, On the Theory of the Brownian Motion, *Phys. Rev.* **36**, 823 (1930).
- [S8] D. T. Gillespie, Exact numerical simulation of the Ornstein-Uhlenbeck process and its integral, *Phys. Rev. E* **54**, 2084 (1996).
- [S9] D. T. Gillespie, The mathematics of Brownian motion and Johnson noise, *Am. J. Phys.* **64**, 225 (1996).
- [S10] J.-M. Cai, B. Naydenov, R. Pfeiffer, L. P. McGuinness, K. D. Jahnke, F. Jelezko, M. B. Plenio, and A. Retzker, Robust dynamical decoupling with concatenated continuous driving, *New J. Phys.* **14**, 113023 (2012).
- [S11] W. von der Linden, V. Dose, and U. von Toussaint, *Bayesian Probability Theory*, (Cambridge University Press, Cambridge, UK, 2014).
- [S12] A. Gelman, J. B. Carlin, and D. B. Rubin, *Bayesian Data Analysis*, 2nd ed. (Chapman&Hall/CRC, 2004).
- [S13] W. R. Gilks, S. Richardson, and D. J. Spiegelhalter, *Markov Chain Monte Carlo in practice*, (Chapman&Hall/CRC, 1996).